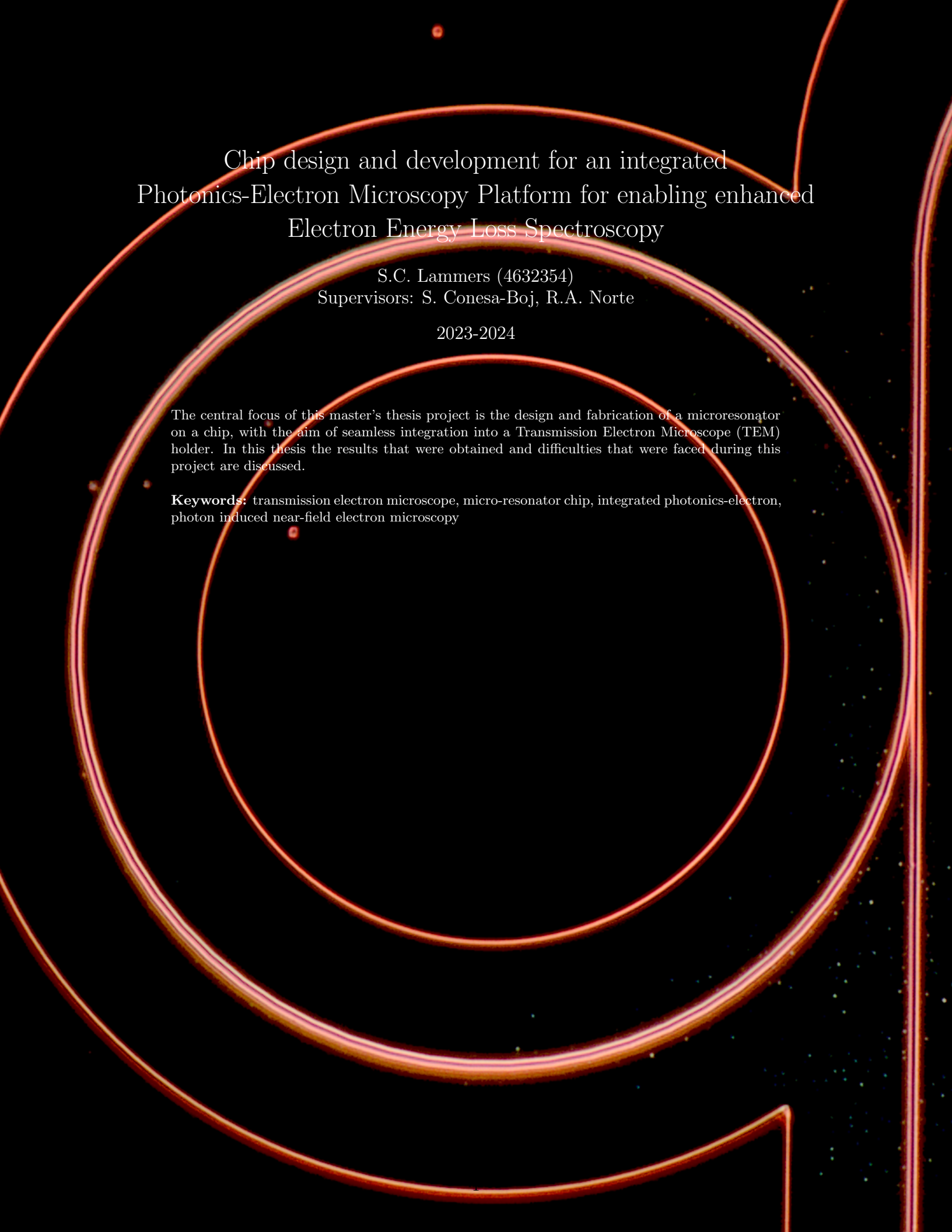


Department of Precision and Microsystems Engineering

Chip design and development for an integrated Photonics-Electron Microscopy Platform for enabling enhanced Electron Energy Loss Spectroscopy

Steven Lammers

Report no : 2024.020
Coach : Richard A. Norte
Professor : Sonia Conesa-Boj
Specialisation : MSD
Type of report : Masters thesis



Chip design and development for an integrated Photonics-Electron Microscopy Platform for enabling enhanced Electron Energy Loss Spectroscopy

S.C. Lammers (4632354)
Supervisors: S. Conesa-Boj, R.A. Norte

2023-2024

The central focus of this master's thesis project is the design and fabrication of a microresonator on a chip, with the aim of seamless integration into a Transmission Electron Microscope (TEM) holder. In this thesis the results that were obtained and difficulties that were faced during this project are discussed.

Keywords: transmission electron microscope, micro-resonator chip, integrated photonics-electron, photon induced near-field electron microscopy

Contents

1	Introduction	4
2	Thesis Scope and Outline	5
3	State-of-the-art	6
3.1	Transmission Electron microscope	6
3.1.1	The monochromator	7
3.2	Microresonator and PINEM Innovations in Electron Microscopy.	8
4	Electron shaping via microresonators	11
4.1	Microresonator theory	11
4.2	Photon Induced Near-Field Electron Microscopy	14
4.3	Non-linearity	15
5	Methodology	16
5.1	Design of the Holder	16
5.2	Optimized Microresonator Parameters in Comsol	18
5.3	Optimized Microresonator Parameters in Rsoft synopsys	19
5.3.1	Bending radius simulation	19
5.3.2	Gapsize simulation	20
5.4	Waveguide simulations	23
5.5	Layers	26
5.5.1	Amorphous silicon top layer	26
5.6	Chip layout	27
5.6.1	The grating pattern	27
6	Electron beam interaction simulations	29
6.1	Electron beam simulation as particles	31
6.2	Electron beam simulation as a wave	32
7	Fabrication methods of the TEM chip	33
7.1	Masks	33
7.2	Deep reactive Ion Etching (DRIE)	34
7.3	Layer deposition methods	35
7.4	Acid cleaning	35
7.5	Inspection methods	35
8	Chip layer design	36
8.1	Klayout pattern	36
8.1.1	Contour layer	36
8.1.2	Optical fiber layer	36
8.1.3	Resonator layer	37
8.1.4	Grating pattern layer	37
9	Fabrication optimization	38
9.1	Amorphous silicon layer deposition	38
9.2	Resist	39
9.3	Electron beam writing	41
9.4	Etching in silicon	42
9.5	Etching in amorphous silicon	42
9.6	Inspection in the NOVA SEM	42
10	Outlook	44
11	Conclusion	45

12 Appendix	49
12.1 Appendix A: UV Lithography method	49
12.1.1 Silicon grass	49
12.1.2 Ebeam pattern generation versus UV lithography pattern generation	51
12.1.3 AMS Bosch etching	51
12.2 Appendix B: Etching settings	52
12.2.1 Oxford Estrelas silicon etching parameters	52
12.2.2 AMS Bosch silicon etching parameters	52
12.2.3 AMS Bosch silicon dioxide/nitride etching parameters	52
12.3 Appendix C: The monochromator	53
12.4 Appendix D: Dose update tests	55
12.4.1 Dose updates in silicon	55
12.4.2 Dose updates in amorphous silicon	56

1 Introduction

Electron energy-loss spectroscopy (EELS) is a powerful analytical technique used in transmission electron microscopy (TEM) to investigate the energy loss of electrons as they interact with a specimen. EELS provides valuable information about the electronic structure, composition, and bonding properties of materials at the nanoscale. Despite its tremendous potential, EELS techniques often face challenges related to spectral resolution and signal-to-noise ratio. In this context, the present project aims to significantly enhance the EELS spectra resolution by innovatively designing and fabricating a specialized Transmission Electron Microscope (TEM) holder. By leveraging advances in photonics and micro-resonator technology, this project seeks to revolutionize the quality and accuracy of EELS measurements, opening new avenues for high-resolution material characterization.

The motivation behind this project lies in the critical need to overcome existing limitations in EELS techniques and push the boundaries of nanoscale material analysis. Traditional EELS setups, while offering valuable insights, often suffer from challenges associated with background noise, limited energy resolution, and compromised signal quality due to multiple scattering events. These factors hinder the ability to extract precise information about material properties, impeding progress in various scientific and technological fields.

Motivated by these challenges, the central aim of this project is **to design and develop a TEM holder that incorporates cutting-edge photonic micro-resonator technology**. This combination is expected to improve EELS abilities. The proposed holder will enable controlled interactions between the electron beam and the photonic micro-resonator, exploiting quantum optical phenomena to enhance the energy-loss signal and reduce unwanted noise. This approach aligns with recent advancements in Photon Induced Near-field Electron Microscopy (PINEM), quantum optics and electron-photon interactions, paving the way for unprecedented sensitivity and resolution in EELS measurements.

The outcomes of this project hold immense promise for diverse scientific disciplines. In materials science, researchers will gain deeper insights into the electronic behavior and properties of nanomaterials, facilitating the design and optimization of advanced materials with tailored functionalities. Additionally, the improved EELS resolution will impact fields such as catalysis, nanoelectronics, and biological imaging, where precise characterization at the nanoscale is essential.

To achieve our objectives, we will address the following key research questions:

- What are the optimal design parameters for the micro-resonator, facilitating efficient electron-photon interactions and maximal photon generation per electron?
- What strategies can be employed to mitigate potential sources of photon loss within the integrated TEM holder, such as losses in coupling, transmission, and detection, thereby maximizing the efficiency of photon collection and measurement?
- How do the characteristics of the micro-resonator, such as its size, shape, and material properties, impact the generation and propagation of cavity photons, and how can these parameters be tailored for optimal EELS performance?

We expect that the results of this project will revolutionize the field of material characterization by enabling unprecedented high-resolution EELS measurements, poised to impact diverse scientific and technological domains.

2 Thesis Scope and Outline

The thesis starts by elaborating on the transmission electron microscope (TEM) which is the intended environment where the design will be operated. The design is a chip which contains an optical microresonator. This chip will be mounted in the TEM using a holder which is essentially a rod that often can also manipulate the chip it is housing. In this thesis the design of a holder and a chip that can manipulate the electron beam through an optical microresonator will be discussed.

Next (in chapter 3.2) the current and relevant developments in the field of optical/ mechanical microresonators are investigated to increase understanding on the topic. This research yielded a number of interesting studies by among others: F. Javier Garcíá et al. [13], R. Shiloh et al. [40], Henke et al [27] and Feist et al. [17]. These studies all utilized different optical methods to manipulate the electron beam and demonstrated that there is a lot of potential in this field.

In chapter 4 the theory of microresonators is discussed and elaborated on. This includes discussions on the Q factor, resonance wavelength, Free spectral range (FSR), full width at half maximum (FWHM), etc., all of which are crucial in understanding microresonators. The theory was collected by investigating different papers that successfully implemented microresonators in their projects. Furthermore the functionality of microresonators is discussed which is essential to understand in order to work on this project.

Next the concept of photon induced near-field electron microscopy (PINEM) is introduced (chapter 4.2). This project attempts to combine PINEM and microresonator phenomenas to modulate the electron beam of a TEM to obtain higher resolution measurements. The optical field that is generated by the microresonator interacts with the electron beam and through energy filtering sidebands in the energy spectrum are revealed that contain extra information about the sample that is studied.

A design for both the holder and the microresonator can be obtained (chapter 5) with this theory and past studies in mind. First of all a design of a TEM holder is introduced which has been modelled in Autodesk Inventor. This TEM holder has been equipped with an optical fiber feed-trough to supply laser light to the chip without breaking the vacuum seal. Furthermore a custom designed tip has been developed that mounts the chip along the electron beam. The geometry of the microresonator has been designed through multiple simulations with the use of Comsol Multiphysics and Rsoft Synopsys. This microresonator has been implemented on a chip that enables an interface between the straight waveguides and the optical fibers with the use of grating couplers.

Simulation strategies for the electron beam have been investigated (chapter 6). There are multiple approaches because of the wave and particle nature of the electron. The electron beam has been simulated as a wave and as a particle. The expectation is that the wave version of the electron beam will be necessary since wave properties have to be evaluated. A simplified model has been created in Comsol which consists only of a segment of the ring resonator to reduce the simulation workload. In this model a perfect coupling has been assumed between the straight waveguide and the ring. This model is considerably more robust than the full ring resonator simulations and the simulation time is low. This model has been used to simulate and has high potential to yield good results.

A lot of time has been invested in the cleanroom fabrication process. This included acid cleaning, spincoating resist, e-beam lithography, SEM inspection, etc.. In Chapter 9, the optimal fabrication parameters, determined through trial and error, are discussed. Dose tests have been performed in the EBPG5200 to find the optimal dose for each of the features in the design. The dose determines how accurate the pattern is transferred to the resist. This varies for different pattern sizes. Furthermore etching in the Estrelas has been done to create resonator geometries in silicon and amorphous silicon. Lastly, in the Outlook chapter, we will present a proposal for future steps.

3 State-of-the-art

3.1 Transmission Electron microscope

The TEM is a high-tech machine that is used to study materials at atomic resolution. It does this with the use of a focused electron beam. These electrons are generated at the top of the microscope in the range of 30 to 300 keV and are subsequently accelerated through a series of magnets (Figure 1). Approximately halfway down the microscope, these electrons encounter the sample, which needs to be exceptionally thin (approximately 400 nm thick) to allow the electrons to pass through it. Upon interacting with the atoms in the sample, the electrons scatter and lose energy. These scattered electron's and their energy levels can be measured by an electron spectrometer in order to identify the atoms [14]. Inserting the sample is facilitated by employing a holder which is essentially a rod. The holder can be introduced from outside the electron microscope into the column, forming an air-tight seal with the microscope housing, and the sample is located at the end of this rod.

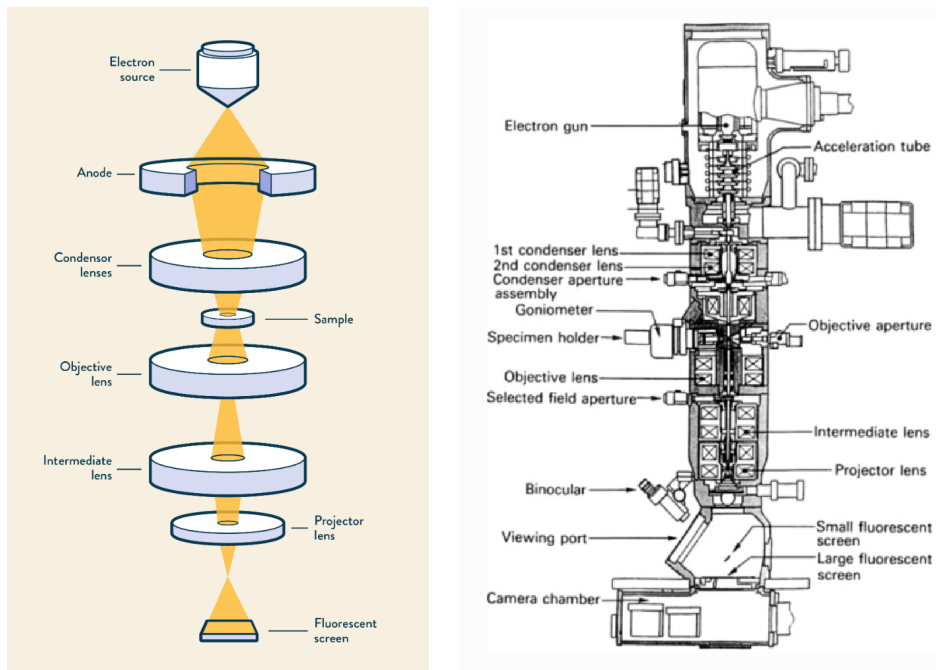


Figure 1: Left: schematic overview of the critical components of a transmission electron microscope [23]. <https://www.technologynetworks.com/analysis/articles/sem-vs-tem-331262>. Right: more detailed cross-section of the TEM [19].

The holder entrance of the electron microscope is called the goniometer. The goniometer can move the holder up to 1 millimeter in each direction (in X,Y and Z). Furthermore it can rotate the holder around its axial direction. This rotation is called the alpha-tilt. The holder not only "holds" the sample but can also be used to manipulate the sample while studying it in the electron microscope. The holder can for example heat or cryogenically cool the sample. The latter is very important for studying biological samples since they need to be contained in an ice layer. Often the sample is contained inside (or on top off) a MEMS chip. This MEMS chip can also be used to manipulate the sample while studying it. This project however, will not use a MEMS chip to manipulate the sample but to manipulate the electron beam.

The inside of the electron microscope consists of a high vacuum (10^{-7} Pa to 10^{-9} Pa). This high vacuum places certain constraints on the MEMS chip that is inserted in the electron microscope. The materials that are used can not gas out or leave behind particles and thus contaminate the vacuum. For example Zinc is known to gas out in high vacuum and cause contamination inside the electron microscope. This can be catastrophic for the up-time of the electron microscope since it will have to be cleaned. Another important aspect of the environment inside the electron microscope are magnetic

fields. The materials must be selected such that no unwanted magnetic fields are created. These magnetic fields disturb the electron beam and can cause the beam to go out of focus or to not go where it is intended at all. Ferro-magnetic materials for example should be avoided.

The spatial resolution is a measure for the contrast and the number of pixels that are present in the image that is created in the TEM [15]. This however depends on multiple variables. One variable for example is the amount of mechanical vibrations that are present in the TEM housing. The TEM is very sensitive to vibrations from external sources like a tram passing by on a track nearby or a door in the laboratory that just closed. Electron microscopes are often placed on foundations that are separated from the foundation of the building where it is located. This is to prevent external vibrations from elsewhere in the building from reaching the TEM. Another variable that compromises the spatial resolution of a TEM are temperature fluctuations. Temperature fluctuations will cause the frame of the TEM to expand or contract and thus to warp. This ruins the alignment of the electron column resulting in a decrease of resolution. Furthermore this can result in "drift" of the sample. This is the phenomena where the location that is studied moves out of view as a result of those expansions or contractions. Another aspect is the optics that are present in the TEM. These consist of mechanically fabricated components that are inherently imperfect due to tolerances on the geometrical dimensions.

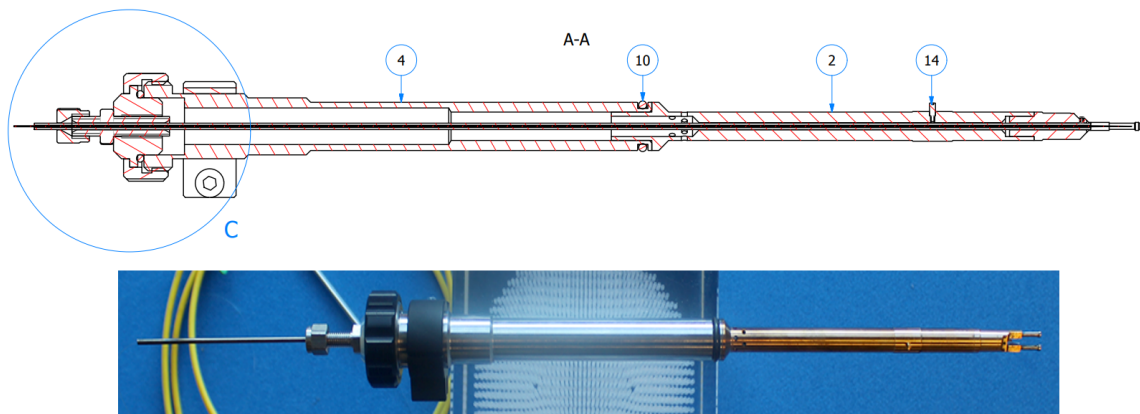


Figure 2: Optical fiber holder from HennyZ that will be modified to test the performance of the microresonator chip. On top there is a technical drawing of the cross section of the optical fiber holder, on the bottom is an actual picture of this holder.

A chip will be manufactured in order to test the performance of the microresonator. A TEM holder is required to mount the chip inside of the TEM. The company HennyZ manufactures holders and will facilitate the holder that will be used for testing. Figure 2 shows the type of holder that will be modified to house the chip. This holder has an optical fiber feed trough from the outside to the tip of the holder where the chip will be housed. The component that mainly needs to be modified is the tip. The holder (Figure 2) currently has a tip that shields a fragile wire that extends out of the holder. The tip will be modified to house a chip of roughly $6 * 3 * 0.5mm$ and a mechanical interface between the optical fiber and the chip.

3.1.1 The monochromator

A current solution to improving the spectral resolution nowadays is by installing a device called a monochromator (see in the appendix 12.3) in the electron gun of the TEM. This device uses a set of electromagnetic lenses to guide the electron beam past a energy selecting slit. The output of the monochromator is an electron beam with a smaller energy spread which reduces the chromatic aberration. This allowed scientists to reduce the full width at half maximum from 0.65 eV to 0.2 eV [25]. A disadvantage of the monochromator however is that the intensity of the electron beam is compromised [24]. Furthermore, the implementation of the monochromator in the TEM is costly and increases the external dimensions.

3.2 Microresonator and PINEM Innovations in Electron Microscopy.

Microresonators help us control light at a very small scale, enhancing our ability to observe and analyze microscopic structures. As the fabrication processes become more widely understood, microresonators are finding increasingly diverse applications, becoming integral tools in advanced fields like electron microscopy. This technology’s potential for precise control and manipulation of light opens new avenues for improving imaging techniques, particularly in the study and analysis of materials at the nanoscale. One such application is the notch-filter. Microresonators are a very compact way to filter out certain wavelengths. Absil et al.[1] propose multiple designs for notch filtering. One design uses a racetrack microresonator. The microresonator is tuned by varying the radius and interaction length in order to achieve resonance at the desired wavelengths. At these wavelengths the signal is filtered out of the spectrum.

Furthermore microresonators have shown promise in gas sensing applications. For example, Eryürek et al. suggest using a disk microresonator with a palladium (*Pd*) sensing layer to detect hydrogen gas (H_2) [16]. This detection method relies on observing changes in the location of waveguide gallery modes (WGM) due to the expansion of the *Pd* layer as palladium hydride forms.

As earlier mentioned, microresonators can also be used as a strain sensor. Microresonators are particularly suitable for this since their performance is very dependent on the geometry of the resonator. The signal changes very noticeably when the geometry changes due to for example strain [6].

In the context a study by Zulio et al., a spiral-shaped microstructure is used to demonstrate the resulting electric field at the center of the structure when exposed to a 633 nm wavelength laser [48] (Figure 3). This study shows that this idea might have some merit to it. Zulio et al. used Comsol Multiphysics to simulate the electric field that is generated.

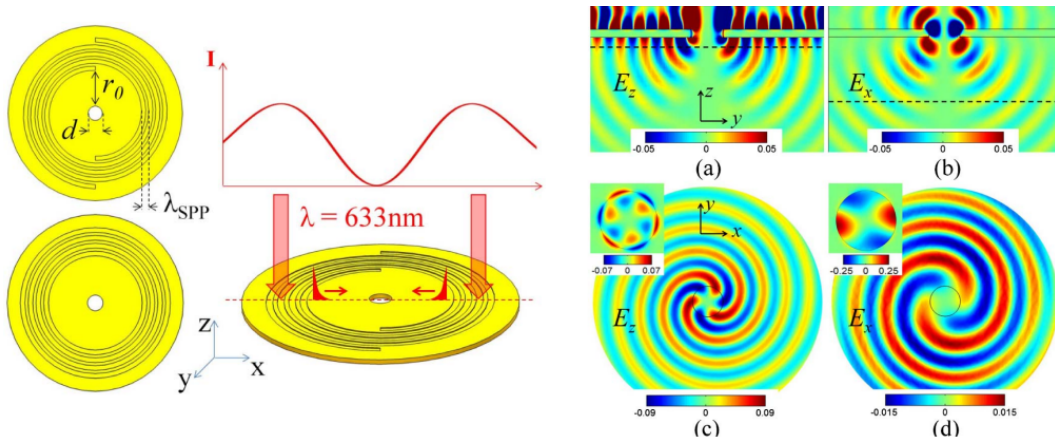


Figure 3: Left: The spiral shaped micro structure and the dimensions. Right: Electric field simulations of the micro structure as a result of the illumination. [48]

Multiple solutions have been found in the field of electron beam manipulation. One of these solutions is to modulate the electron beam directly with the phase of a laser. The plane, that is traversed by the electron beam, is exposed by the laser. The plane reflects the light along the electron beam in a parabolic mirror that refocuses the light. The phase of the light is in this way imprinted on the electron beam (see Figure 4). This setup does however require multiple elements to be installed in the TEM.

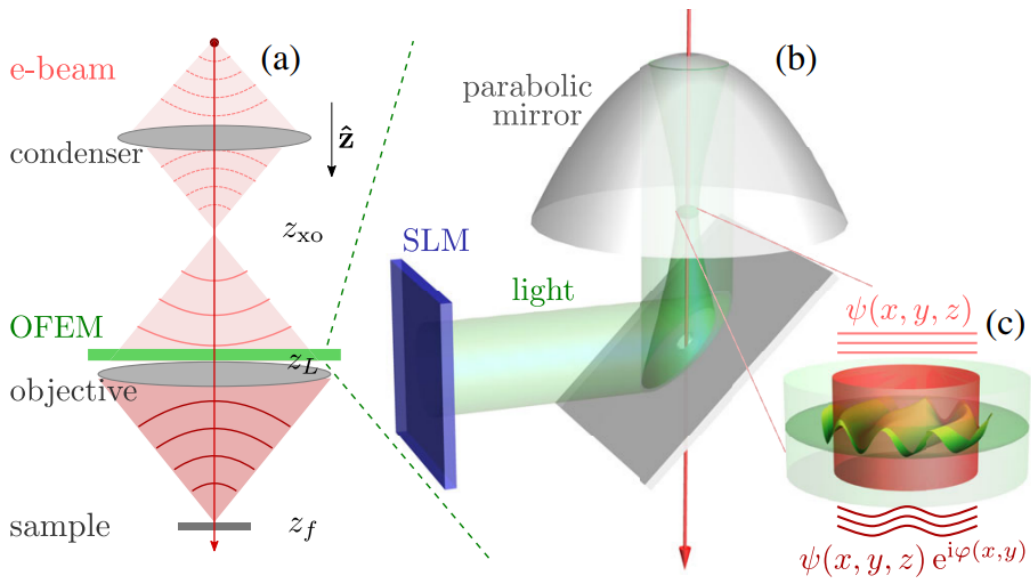


Figure 4: Optical free-space electron modulator (OFEM). a) The components that are placed in the electron microscope column, b) The spatial light modulator (SLM) shines onto a tilted plane that is traversed by the electron beam. The light is deflected along the electron beam into a parabolic mirror. c) The light phase that is imprinted on the electron beam. [13]

PINEM has been applied in the Scanning Electron Microscope (SEM) too. PINEM experiments are easier to conduct in a SEM than in a TEM as the SEM is smaller, cheaper and easier to operate. Furthermore the electron energy in a SEM is lower than in a TEM which results in a lower velocity of the electrons making it easier to interact with the electrons [33, 43]. All these benefits inspired R. Shilloh et al. to investigate PINEM in a SEM. This study stands out because Shilloh et al. modified a SEM and implemented a commercially build EELS detector in the SEM allowing them to measure the electron energy spectrum from back scattered electrons (see Figure 5). The electron beam modulation was realised by illuminating a tungsten tip which is positioned closely to the electron beam. The illumination was done by a 1030 nm wavelength laser.

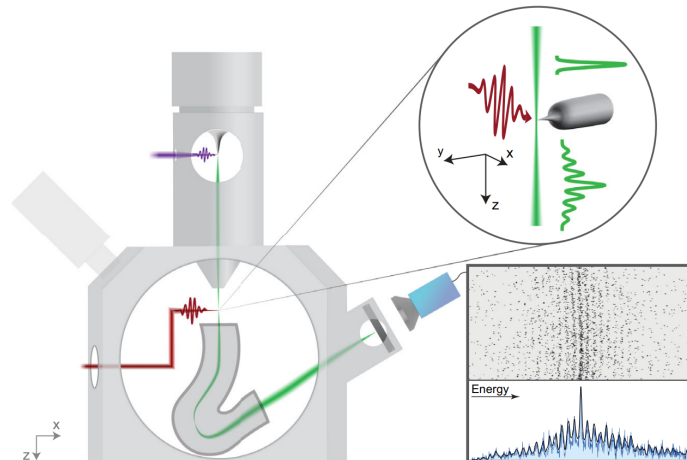


Figure 5: A cross section of the modified SEM showing the implementation of an EELS detector [40].

A paper that inspired this project is a study by Henke et al. [27]. In this study a TEM holder was manufactured with an integrated microresonator that was used to modulate the electron beam. The microresonator is positioned parallel to the electron beam. This causes the optical field to intersect with the electron beam. The optical field in turn exchanges photons with the electrons causing them

to lose or gain energy and thus modulate. It demonstrated the feasibility of this method. The aim of this project is to recreate and improve on this design. Figure 6 shows the setup that was created for this study. This study however did not include samples in the setup.

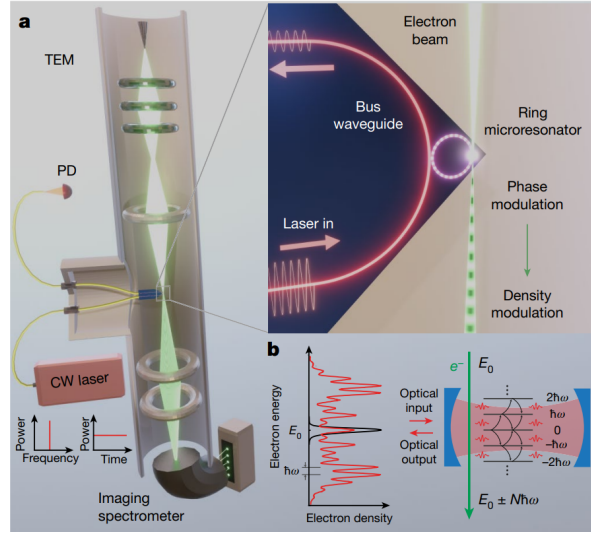


Figure 6: a) A cross section of the TEM showing the critical components of the setup. The top right shows the waveguide and resonator structure that was realised. b) The electron energy spectrum that show the revealed energy side-bands after modulation of the electron beam [27].

A recent study by Feist et al. showed a setup (Figure 7) that uses a metallic sheet that is traversed by the electron beam. The sheet is illuminated by a laser that creates a pattern of plasmons. These plasmons in turn generate an optical field that is imprinted on the electron beam. The setup allowed control over the pattern of the plasmons as well as control over the shape of the laser beam. The authors used this to control the shape of the optical mode. The optical field locally increases the electron velocity and thus the electron energy. This increased energy can be observed during the post-processing of the images as can be seen in Figure 7. The figure shows the control over the electron beam that the authors are trying to achieve.

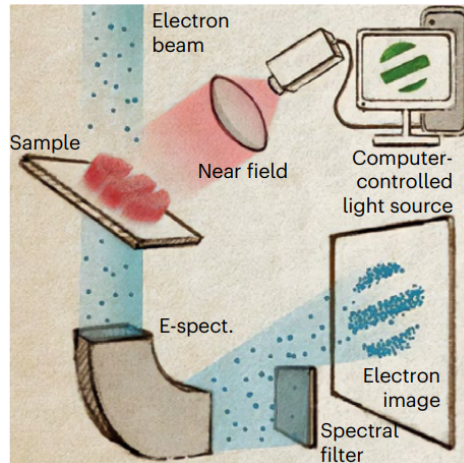


Figure 7: Setup that is used by Feist et al. to imprint a profile onto the electron beam [17].

4 Electron shaping via microresonators

4.1 Microresonator theory

A microresonator is a structure (Figure 8) in the micrometer range that is designed to create resonance at a certain specified wavelength of light. The structure usually consists of a waveguide that transports light in and out of the system. The waveguide transports light through total internal reflection which results in light confinement. This means that the refractive index contrast between the silicon waveguide and the upper/lower layer is sufficiently large to allow total internal reflection. A bigger contrast in refractive indices allows for a tighter radius of the resonator ring. Somewhere along the waveguide a resonator is positioned. This resonator can be any loop shaped waveguide but usually it is ring shaped. The incoming light couples through a gap to the resonator causing a fraction of the light to propagate to the resonator. The light will then start traveling along the resonator and will eventually dissipate due to internal losses and a part will also couple back to the waveguide. At resonance, constructive interference causes a build up of wave amplitude. Resonance occurs when the optical length of the resonator is an integer multiple of the wavelength. At resonance (assuming critical coupling) the incoming lightwave almost fully couples to the resonator and the outgoing light wave will have an amplitude of almost zero. Figure 8 describes the components of an ordinary ring microresonator and the terminology that is used. The coefficients K and K' represents respectively the loss coefficient of the coupling from the waveguide to the resonator and the loss coefficient of the coupling from the resonator to the waveguide. The self coupling coefficient (r) and the intrinsic loss coefficient in the resonator (a) are also depicted in the figure.

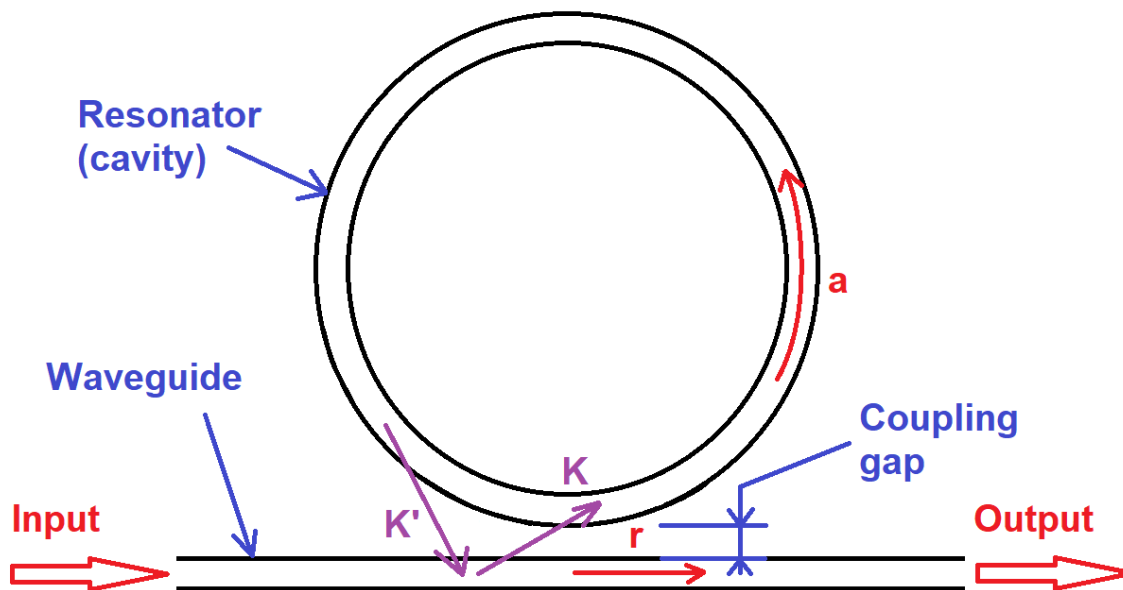


Figure 8: Interaction losses of the waveguide to the resonator where r is the self coupling coefficient, a the internal loss ratio, K the coupling losses from the waveguide to the resonator and K' the coupling losses from the resonator to the waveguide.

The wavelength at which resonance occurs is strongly dependent on the geometry of the microresonator. Small changes in the geometry will cause the resonance wavelength to shift. Critical coupling is achieved once the intrinsic loss coefficient a is equal to the self coupling coefficient r . In this case the coupling ratio is given by equation 1.

$$K^2 + a^2 = 1 \quad (1)$$

This phenomena can be exploited to perform very accurate measurements since any perturbation that changes the geometrie of the microresonator can be measured by monitoring the wave amplitude of the output signal. Small geometrical deviations will have a strong effect on the output signal. In this way microresonators can be tuned to pick up for example soundwave frequencies or to measure forces as a strain sensor. Another application can be as a notch-filter. It is also considered to be an all-pass filter [8] since all the wavelengths that are not near resonance wavelnghts will pass the resonator relatively unhindered. Only very specific wavelengths will become fully coupled to the resonator and will thus be "filtered out" from the wavelength spectrum in the waveguide.

Microresonators are prone to non-linear effects. This can be caused by heating of the resonator due to the power that is supplied by the waveguide. The heating effect that is caused by absorbing power will cause the geometry to slightly change due to warpage. This will hinder the functionality due to a shift in the resonance wavelength [34]. One possibility to reduce these effects is by limiting the required input power by reducing the internal losses of the microresonator. There are multiple sources of internal losses: Surface-roughness-induced scattering loss, Scattering loss in the coupling gap spacing, Optical leakage from the undercladding layer, Linear surface-state absorption (SSA) and Nonlinear two-photon absorption (TPA) in silicon bulk [18]. The Surface-roughness-induced scattering loss can be partially mitigated by making sure that the surface roughness of the waveguides are as low as possible. This is a direct result of the production technique that is chosen. Another way of reducing the surface scattering loss would be to reduce the total waveguide length since there would be less surface area for scattering to occur. Irregular features also increase scattering losses. This is specially prevalent in for example the multi mode racetrack resonator which will be discussed later. The coupling gap (between the straight waveguide and the resonator) (Figure 8) is another source of scattering losses. A smaller gap results in less scattering losses since there is less bulk material for the photons to cross. This directly affects the coupling strength between the straight waveguide and the resonator [46].

The performance of a microresonator must be qualitatively measured in order to compare it to other microresonators. The quality factor (Q factor) describes the relation between the stored energy and the amount of energy that is lost (Equation 2)[18].

$$Q = 2\pi \frac{\text{stored energy}}{\text{energy loss per round trip}} \quad (2)$$

The Q factor is thus a measure for efficiency of the microresonator. A high Q factor implies a high efficiency and thus the required optical power is minimized [30]. This definition of the Q factor (Equation 2) does explain the concept but is not very concrete. Another way of evaluating the Q factor is by determining the transmission of the microresonator. The transmission is a measure for the ratio between the optical power that is entering the waveguide and the optical power that is leaving the waveguide. A transmission of zero indicates that all the light at the resonance wavelength is coupled from the straight waveguide to the microresonator. At the resonance wavelength the transmission spectrum then shows a sharp valley. The FWHM (Full Width at Half Maximum) (Equation 7) can be measured of this valley. This too can be used to determine the Q factor (Equation 3) [8].

$$Q = \frac{\lambda_{res}}{FWHM} \quad (3)$$

$$\lambda_{res} = \frac{Ln_{eff}}{m} \quad (4)$$

This definition (Equation 3) is convenient since it is relatively simple to determine the transmission

spectrum from a microresonator design in simulation software like Comsol Multiphysics or Rsoft from Synopsys. The resonance wavelength (Equation 4 [28, 8]) is dependent on the effective refractive index (n_{eff}), the optical length (L) and the order of the mode (m). The optical length is defined as the length of the circumference of the ring ($L = 2\pi R$). Figure 9 shows an example of determining the Q factor from a transmission spectrum. This transmission spectrum has been obtained in Comsol Multiphysics from a ring microresonator that was used in a standard tutorial. Note that the transmission graph is plotted with a normalized y axis ranging from 0 to 1. Here 1 implies complete transmittance from port 1 to 2 and 0 implies no transmittance from port 1 to port 2.

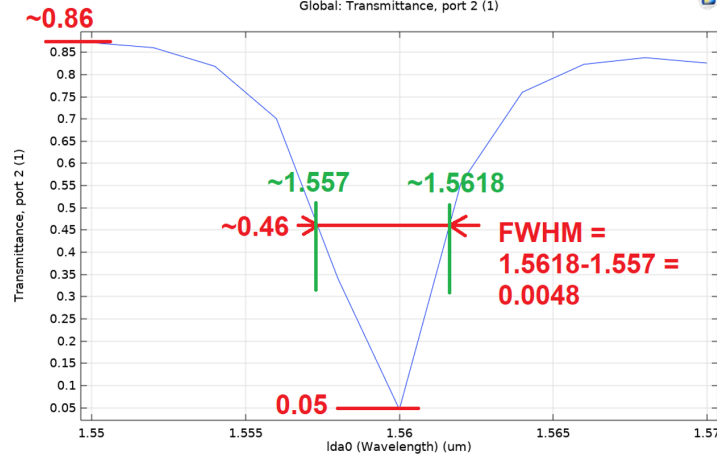


Figure 9: FWHM (Full Width at Half Maximum) determined from a transmission spectrum obtained from Comsol Multiphysics from an arbitrary ring resonator.

Microresonators have multiple resonance wavelengths since they are integer multiples of the optical path length. The distance between neighboring resonance wavelengths is called the Free Spectral Range (FSR) (Equation 5).

$$FSR = \frac{\lambda^2}{n_g L} \quad (5)$$

Where n_g is the group index and L the optical length which is defined as the perimeter length according to Azuelos et al. [3]. The free spectral range (FSR) can be used to determine the finesse. The finesse can also be evaluated to determine the performance of a microresonator (Equation 6) [8, 28].

$$Finesse = \frac{FSR}{FWHM} \quad (6)$$

The FWHM can also be calculated. The definition of the FWHM can be seen in Equation 7. It can be seen that the FWHM depends strongly on the coupling coefficient (r) and the intrinsic loss coefficient (a). The resonance wavelength (λ_{res}) has a quadratic relation with respect to the FWHM.

$$FWHM = \frac{(1 - ra)\lambda_{res}^2}{n_g \pi \sqrt{ra} L} \quad (7)$$

Furthermore the group index (n_g) is used instead of the effective index (n_{eff}) because the group index takes the dispersion in the waveguide into account [8]. The group index is defined as:

$$n_g = n_{eff} - \lambda_0 \frac{dn_{eff}}{d\lambda} \quad (8)$$

The term $\frac{dn_{eff}}{d\lambda}$ is the chromatic dispersion. This value describes how much the effective refractive index changes per change of wavelength. This is a specific value for each material.

4.2 Photon Induced Near-Field Electron Microscopy

The immense potential of electron beams as probing tools has been a source of fascination for scientists throughout history. Yet, a pivotal question persists: *Can we elevate the capabilities of electron microscopy to even greater heights?*

The basic idea is making the fusion of free-electron beams and the optical whispering-gallery modes intrinsic to dielectric microresonators. Due to the interaction between the free-electron beams and the optical whispering-gallery modes of dielectric microresonators, the phase (or timing) of the electrons' motion gets altered in a changing and dynamic manner as they move together. This modulation affects how the electrons behave as they travel alongside the optical modes, introducing fluctuations in their phase relationships.

A microresonator can have multiple modes, which refer to different ways in which light or electromagnetic waves can circulate within the resonator. The exact number of modes depends on various factors, including the geometry and material properties of the microresonator. In the context of whispering gallery modes in dielectric microresonators, there can be numerous modes with distinct resonant frequencies and spatial distributions, each corresponding to a different way that light can travel around the resonator's curved surface. The modes are characterized by their unique resonance frequencies and associated electromagnetic field patterns.

The electron microscope creates images based on elastic interactions between an electron and the matter that is studied. During these interactions there is no energy loss or gain. Electron spectroscopy however makes use of inelastic electron interaction. During these interactions there is energy loss due to excitation of matter. Electron energy loss spectroscopy (EELS) analyses these energy losses to obtain information about the sample. Electron wavepackets have a specific energy spectra after interaction with the sample. During "normal" unaltered imaging the zero loss peak is dominant. However, a photon induced field can filter out the zero loss peak to reveal energy side bands which contain extra information (Figure 10). Furthermore the full width at half maximum (FWHM) of the zero-loss peak is reduced which is directly related to the resolution [2]. This process is called energy filtering. The side bands are separated from the initial energy by integer multiples of the photon energy [27]. The imaging can be done based on those side bands with high spatial resolution [27, 15]. Furthermore, this technique can be used to for example visualize the evanescent electrical field [4].

The interaction between the micro structure and the electron beam is caused by the optical field as a result of generated plasmons. Plasmons are free electrons that are excited as a result of illumination by light. These plasmons in turn generate electromagnetic waves on the surface of the structure that are called surface-plasmon polaritons (SPPs) [45]. The shape of the micro structure defines the shape of the optical field that is generated by the SPPs and thus the shape that is imprinted on the electron beam.

The process of using a photon induced (optical) field to manipulate the electron beam is called Photon-Induced Near-field Electron Microscopy (PINEM) [13]. PINEM can be achieved by using a laser to shoot pulses into the electron beam or on a membrane that is in close proximity to the electron beam [35]. The electron wavepackets and the optical field exchange photons through inelastic interaction. The electron accelerates or decelerates as it exchanges photons with the optical field. This interaction can happen many times as the energy of the wavepacket is much larger than the net energy change induced by a single photon [40, 12]. The photons that an electron wavepacket can exchange are generated through the Smith-Purcell effect [47, 36] as the wavepacket moves close to material boundaries. This process allows manipulation of the electron beam through an optical field. Such an optical field can be generated through photonic micro structures like microresonators. B. Barwich et al. used PINEM and have created a plot (Figure 10) showing the influence of a photon pulse on the electron energy spectra of an electron wavepacket. The plot shows that energy side bands are revealed once the zero loss peak is more or less filtered out. The black plot is the energy spectra of an electron wavepacket before interaction with a photon pulse. It can be observed from the red plot that extra energy peaks are revealed.

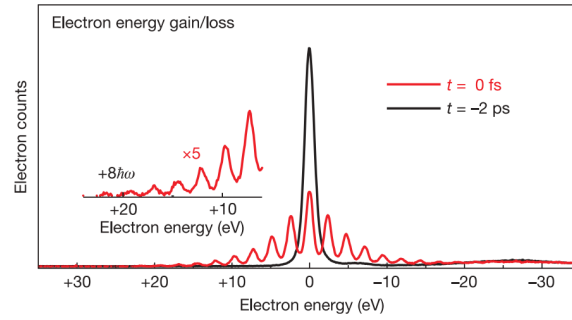


Figure 10: Plot showing the electron energy versus the electron counts. The black plot shows the electron energy spectra before the photon pulse and the red plot shows the electron energy spectra after the photon pulse [4].

4.3 Non-linearity

Microresonators are sensitive to non-linear effects. These non-linear effects can be caused by warping of the resonator geometry due to induced heat by the optical power that is absorbed. This induced heat causes the resonance peak to skew and thus a shift of the resonance wavelength. This effect is very undesirable since it hinders the ability to effectively operate the microresonator. This issue motivates the design of a high Q-factor microresonator since a high Q-factor implies low energy losses and thus lower required optical power. Figure 11 shows the non-linear effect of increased power to the transmission spectrum. It also shows an hysteresis effect on the input versus the output power.

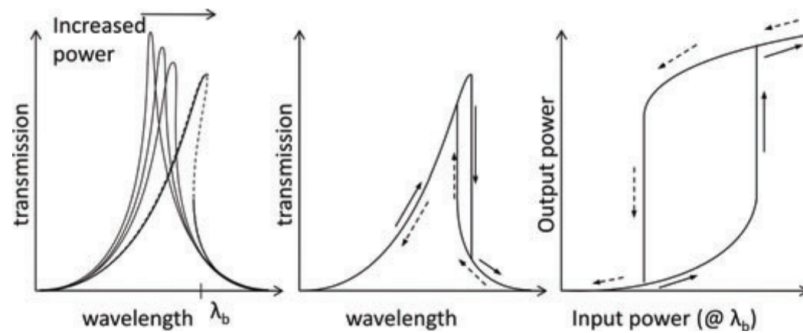


Figure 11: left) Skewing of the resonance peak as the power is increased. middle,right) hysteresis effects as a result of the increased input power[8].

5 Methodology

The core experimental work for this project will be carried out within the Kavli Nanolab's clean room. The upcoming methodology section will outline the specific steps and procedures that will be followed.

5.1 Design of the Holder

As previously mentioned in this report, the holder (Figure 12) is a rod that is inserted in the TEM to position the sample along the electron beam trajectory. The holder serves multiple purposes:

- Rough positioning of the sample with respect to the electron beam.
- Forming a vacuum tight seal with the TEM.
- Manipulation of the sample during or in between measurements.

The manipulation of the sample can be achieved by designing mechanisms within the geometric restrictions of the holder. These mechanisms can be electronically operated or manually operated. The available space for included mechanisms can be limited to a height of only $2mm$. This poses big challenges for both the designer and the fabrication of the holder.

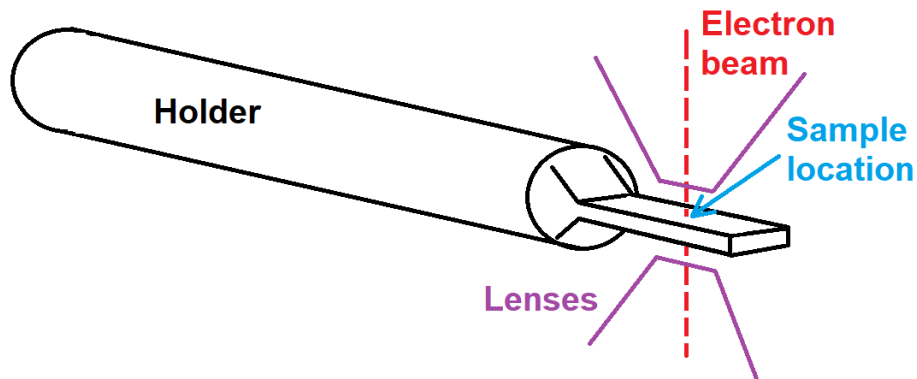


Figure 12: A schematic overview of the transmission electron microscope holder. The sample and lens positions are depicted.

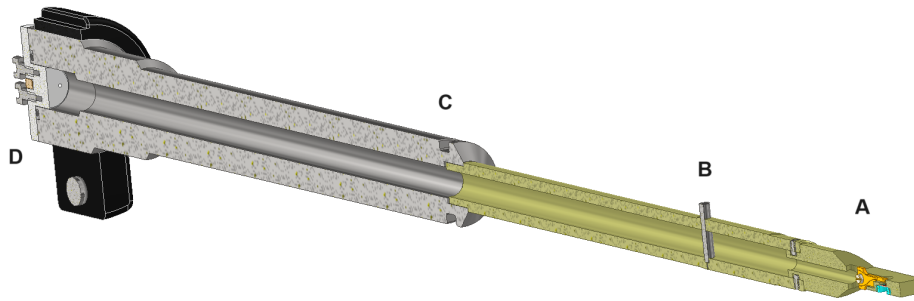


Figure 13: An overview of the microresonator holder that has been designed for this project. The following features are emphasized in this overview: A) The tip where the microresonator is mounted, B) The pin to align the holder within the TEM, C) O-ring groove for the formation of the vacuum seal, D) Optical fiber feedthrough.

The microresonator holder (Figure 13) is a relatively simple holder. The microresonator chip is mounted to the tip. The chip has a specific shape that is dictated by the geometric constraints imposed by the TEM lenses. The optical fibers need to be inserted into the holder to establish a connection between the chip and the laser source. An optical fiber feed trough has been designed to form a vacuum tight seal between the holder and the fibers.

5.2 Optimized Microresonator Parameters in Comsol

There are a couple of tutorials on the website of Comsol about microresonators. These tutorials focus on different aspects of microresonators. One of the tutorials simulate the electric field that is generated in the microresonator as a function of the input power and the input wavelength. The resonances can be identified by looking at the transmission spectrum of the microresonator from port 1 to port 2 by sweeping over the wavelengths of the input light. At the resonance wavelengths the transmittance graph will show a sharp valley where the transmittance approaches zero. One example of a simulation of the electric field of a ring microresonator in resonance is seen in Figure 14.

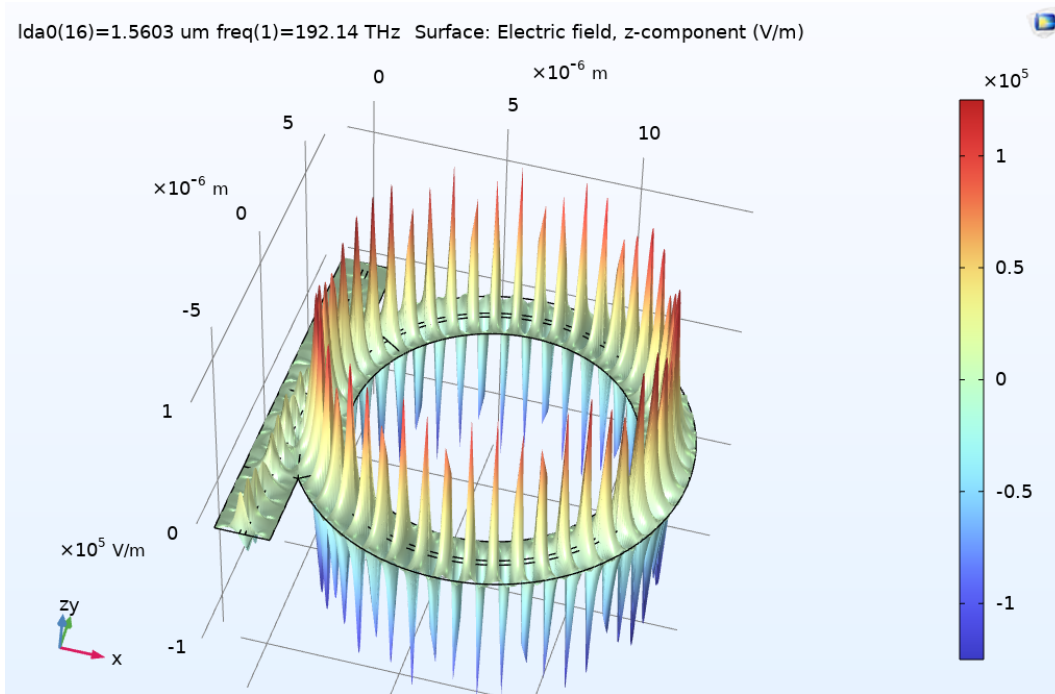


Figure 14: Simulation of the electric field of a ring microresonator at a fixed wavelength. The rectangular shape to the left is the waveguide that forms the input (bottom left) and output (top left) of the lightwave. The ring to the right is the microresonator (cavity) to which the light is coupled.

It can be seen that the incoming light wave (consisting of a single wavelength) is almost fully coupled to the resonator since the wave amplitude at the output is very close to zero. Furthermore the amplitude in the resonator is visibly much higher than the amplitude at the input. This is because constructive interference is occurring between the waveguide and the resonator. This builds up a stronger electric field in the resonator.

The transmission spectrum can be plotted from this simulation (Figure 9). This is done by sweeping the input wavelengths and plotting a graph with on the y axis the transmittance and on the x axis the wavelengths. A close approximation to the resonance wavelength can be found by iterating increasingly small ranges that contain the resonance wavelength. In this way the resonance wavelength value will become increasingly accurate. Another way is to design for a specific wavelength by evaluating equations 2-6.

The resonance wavelength can be selected based on the laser generator that is available. The dimensions of a microresonator can be determined once a wavelength has been selected. First the waveguide has to be designed. The waveguide dimensions determine the mode shape that will be present. This will determine the effective index that will be used for simulation. The resonance dimensions for this wavelength and effective index can be determined by sweeping the outer radius of the microresonator and observing the transmission in the output port. Figure 19 shows an example geometry that has been used to create such a plot and the resulting graph.

5.3 Optimized Microresonator Parameters in Rsoft synopsis

This chapter describes the design process of the microresonator and chip design. The design is based on Comsol and Rsoft Synopsis simulations and practical findings from relevant studies.

5.3.1 Bending radius simulation

The diameter of the resonator determines largely the losses that occur in the ring resonator and determines the optical path length. This optical path length needs to be an integer multiple of the light wavelength in order to cause resonance [18]. A smaller diameter results in more scattering losses and may result in a loss of light confinement if the contrast in refractive indices is not sufficient. The simulations from Rsoft Synopsis support the claim that a smaller radius results in more losses which are a function of the imaginary part of the effective index. The resulting graph of the simulation (Figure 15) is based on a study by Bogaerts et al. [8] where the equation for the bending radius losses is derived. The graph shows that a larger bending radius will lead to a smaller imaginary component of the effective index. This will lead to smaller bending losses since the imaginary component of the effective index and the bending losses are positively related. It can be seen that a bending radius larger than 50 micron minimizes the losses.

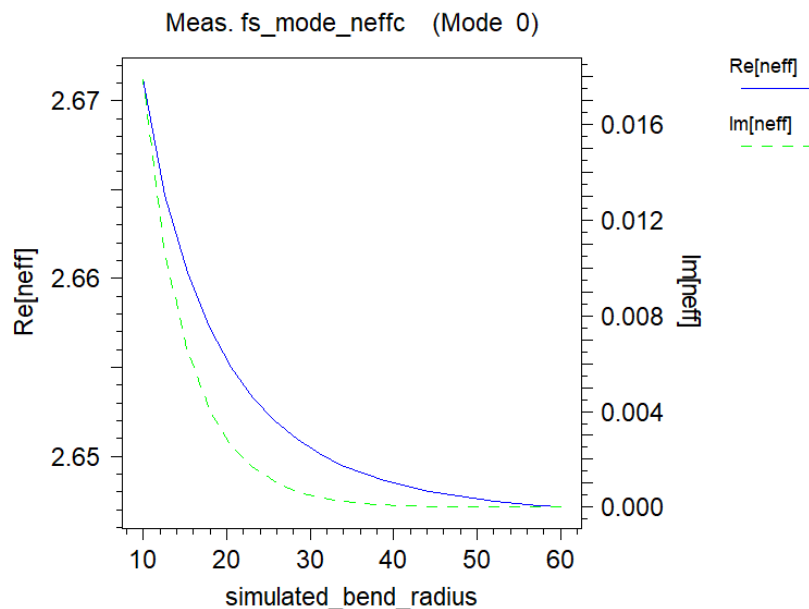


Figure 15: Plot of the simulation result of Rsoft Synopsis on the bending radius of the ring resonator versus the losses that accumulate.

5.3.2 Gapsize simulation

The gapsize is another critical dimension that needs to be simulated in order to find the optimal solution. A waveguide and ring geometry has been created in Rsoft Synopsys in order to investigate the photonic properties as the dimensions are adjusted. The geometry that has been created can be seen in figure 16. The model is fully parameterized such that optimization sweeps can easily be performed. The ring that has been chosen has an outer radius of $50\mu m$ and a height of $0.22\mu m$. The waveguide width is chosen to be $0.49\mu m$. These parameters are kept constant during the gap size simulation. The value that will be evaluated to estimate the gap size is the transmission. This indicates the amount of light that is reaching port 2 from port 1. A transmission of 0 indicates that all the light of the specific wavelength is coupled to the ring resonator. Similarly a transmission of 1 indicates that none of the light in the straight waveguide is coupled to the ring. The resulting graph of the gap size simulation can be seen in Figure 17. The optimal gap size for this geometry and material choice is found to be roughly $0.25\mu m$. Furthermore the coupling has been simulated which can be seen in Figure 18. The amplitude after the ring is almost zero which means that most of the light is coupled to the ring resonator.

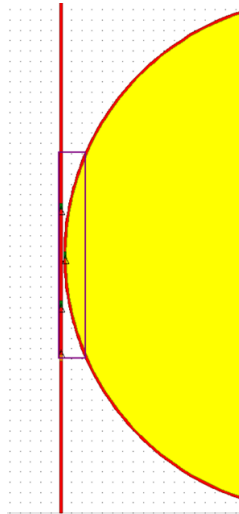


Figure 16: The ring and waveguide geometry that has been created in Rsoft Synopsys to simulate the photonic properties. Note that part of the ring is not showing as a result of zooming in to show the details. The red lines are the waveguides made of amorphous silicon. The yellow area is material with identical properties to the background.

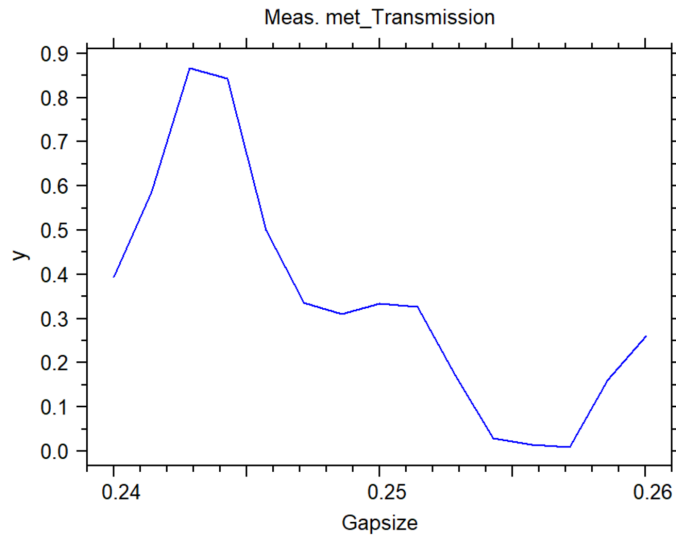


Figure 17: Plot of the simulation result of Rsoft synopsys on the gap size as a function of light transmission from port 1 to port 2.

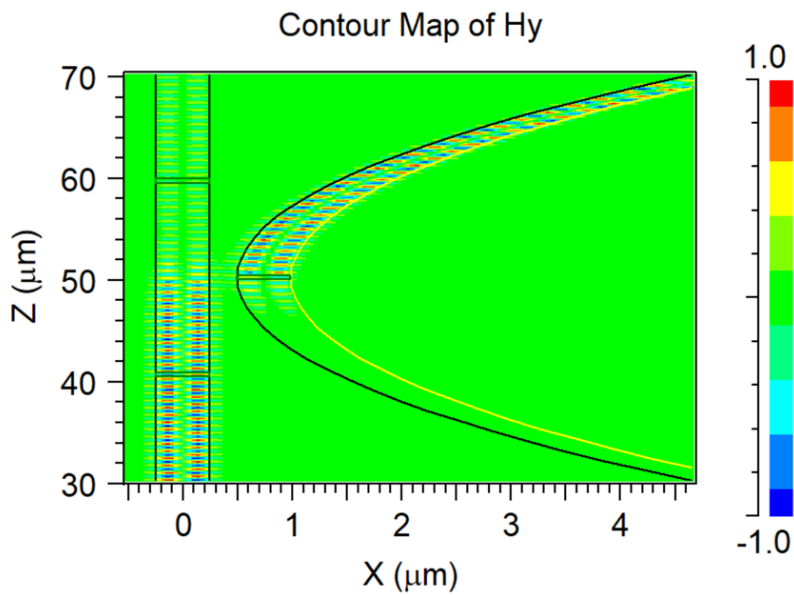


Figure 18: Simulation made in Rsoft Synopsys showing coupling of the light between the straight waveguide and the ring resonator.

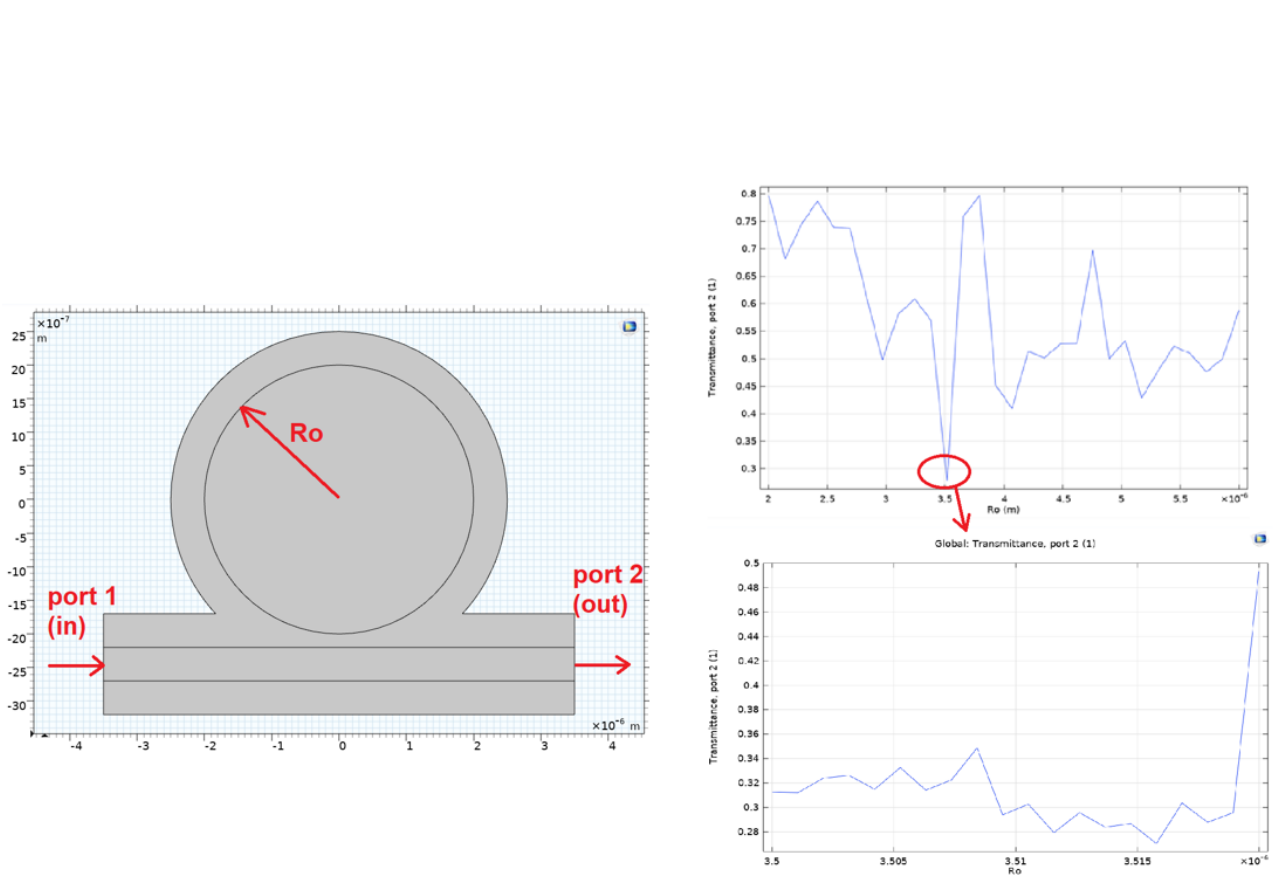


Figure 19: Left: Geometry of the disk microresonator that has been used to perform an outer radius sweep to find the outer radius where resonance occurs. Right: Resulting plot of the outer radius (R_o) sweep of the geometry (that is shown in Figure 19) versus the transmittance. First a rough outer radius sweep (R_o) is performed (top image) and then a much finer outer radius sweep is performed (bottom image) to find a more precise outer radius.

5.4 Waveguide simulations

The waveguide dimensions have a big influence on the effective index n_{eff} which is seen in equation 8. The dimensions must be determined through simulations and with the requirements of the microresonator in mind. There is a Comsol tutorial available that simulates the mode shapes of the optical field of the waveguide and the resulting effective index (Figure 20). Comsol and Rsoft Synopsys will be used to determine the optimal waveguide dimensions for this project.

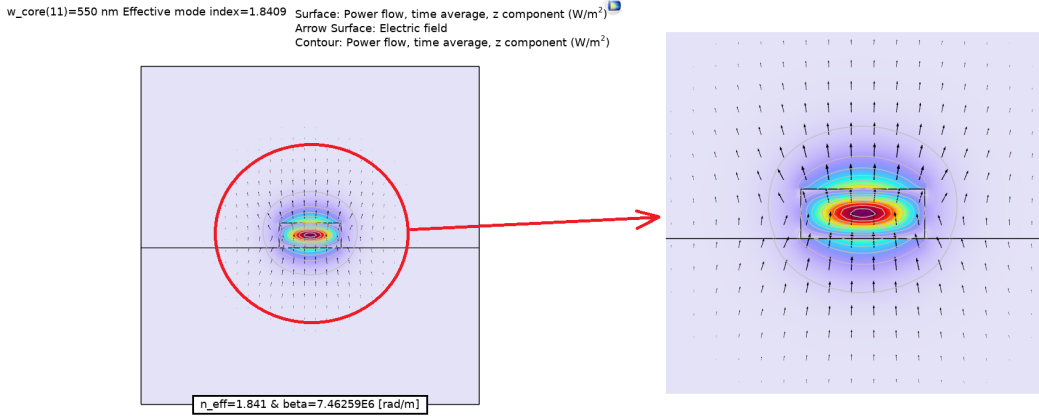


Figure 20: Plot of the simulation result of the Comsol tutorial. The figure shows the mode profile in the waveguide. Multiple waveguide shapes are evaluated in this tutorial.

The waveguide geometry has to be tuned in such a way that the resulting optical field is oriented along the electron beam trajectory. There are, among others, two other mode types that are investigated in this study namely TM and TE modes. The distinction between these modes is the orientation of electric and magnetic field wave vectors. For TM modes the magnetic field vector is oriented perpendicular to the direction of propagation. For TE modes the electric field vector is perpendicular to the direction of propagation. The study conducted by Henke et al. [27] utilizes a quasi-TM mode. It is suspected that the term quasi-TM refers to the fact that the mode is neither purely TM or TE but mostly TM mode and partially TE. Given the success of the approach by Henke et al. it is decided to design a TM mode waveguide for the initial tests. It is desired to find waveguide dimensions such that only one mode is guided to prevent interference from higher order modes. These dimensions are also dependent on the layers that are selected for the chip. For this project the layer composition is a silicon substrate with a silicon oxide layer of $3\mu m$ and a device layer of amorphous silicon of $220nm$ and "vacuum" top cladding. An online simulator has been used to find dimensions that only support a single TM mode. For these settings a plot of the evanescent field has been generated (Figure 21 and Figure 22).

The dimensions that have been chosen such that the evanescent field vertical component is as large as possible. Increasing the width gives rise to higher order modes that can cause modal coupling to occur. Modal coupling transfers the power of one mode to another. This means that the power is shared between multiple modes which causes the desired mode to be compromised in power [20, 29]. This is why it is important to choose a width that only supports one mode. A simulation has been performed that evaluates the modes that are supported by the waveguide as a function of the width (Figure 23). Furthermore it can be observed that the fundamental mode is a TE mode. This can however be filtered out at the light source since we are only interested in the TM modes. The width must be chosen such that the first TM mode is dominant without supporting the second TM mode.

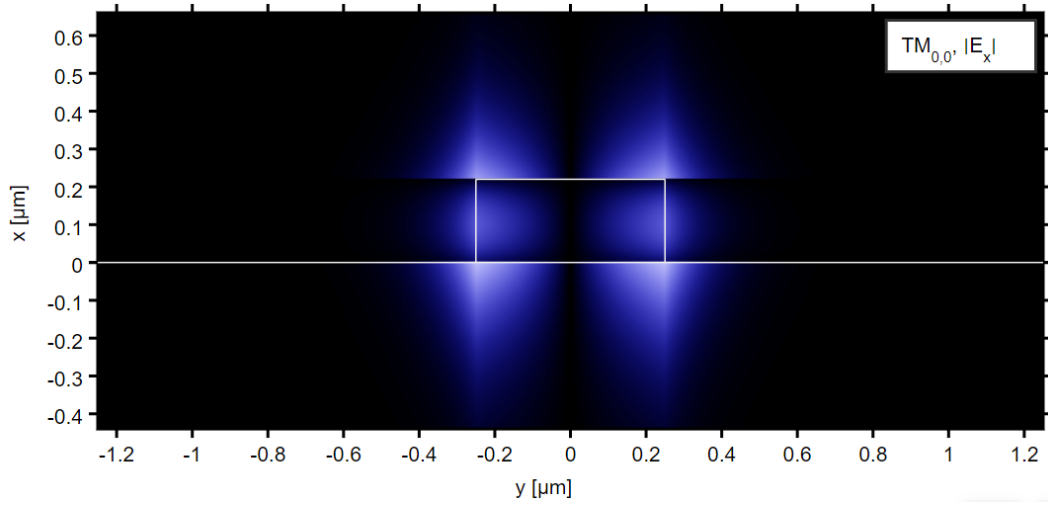


Figure 21: Plot of the simulation result of evanescent field generated by online simulation <https://www.computational-photonics.eu/eims.html>

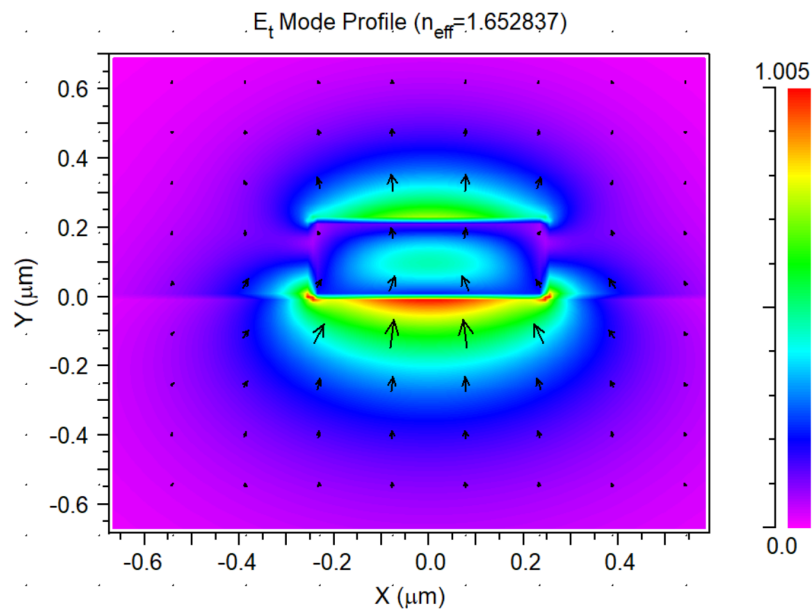


Figure 22: Plot of the simulation result of the mode shape in Rsoft Synopsys. The vertically aligned arrows indicate that this mode is a TM mode.

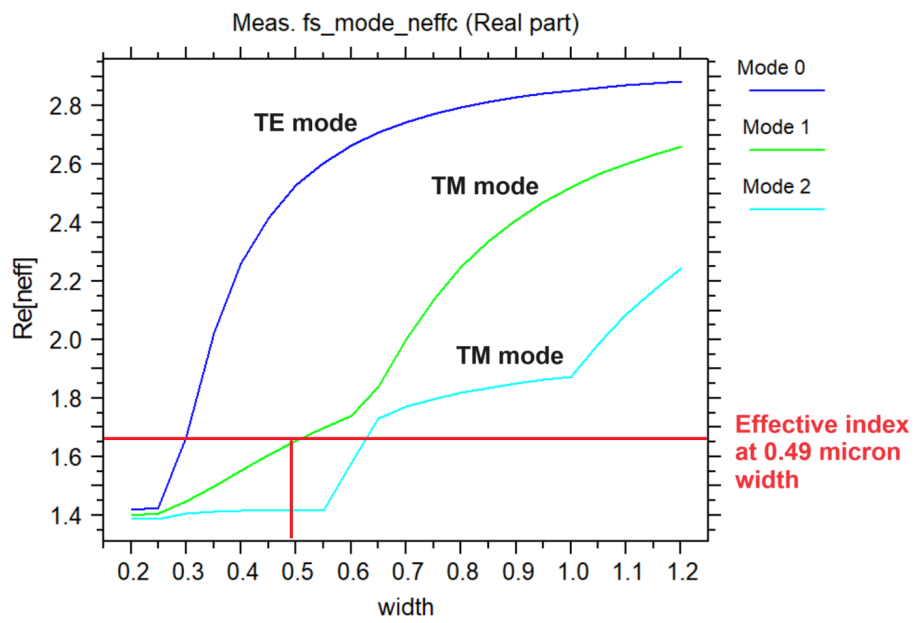


Figure 23: Plot made in Rsoft Synopsys of the effective index of the modes versus the width of the waveguide.

5.5 Layers

The chip will be build up from multiple layers to enable fabrication of the microresonator. The first layer will be the silicon wafer. On top of this silicon a layer of silicon dioxide (SiO_2) will be deposited. This layer serves the purpose to electrically isolate the device layer from the silicon wafer. Furthermore the refractive layer contrast must be as large as possible to ensure proper light confinement in the device layer. Silicon dioxide has a refractive index of roughly 1.5 and Silicon has a refractive index of roughly 3.9. Amorphous silicon will be deposited on top of the silicon dioxide. This layer (device layer) will be etched to fabricate the microresonator. Lastly a top (cladding) layer should be chosen with sufficient refractive index contrast with respect to the device layer. This can be chosen to be "vacuum" cladding since this has a relatively low refractive index of 1.

5.5.1 Amorphous silicon top layer

Silicon on insulator (SOI) wafers are in big demand nowadays which makes ordering them a lengthy and costly process. These wafers have crystalline silicon top layers which require very specific fabrication techniques which are not present in the Kavli cleanroom. These arguments motivated the search for alternative top layer materials. The main consideration is the possibility of fabrication in the Kavli cleanroom. This will simultaneously give the additional benefit of great flexibility. The freedom of layer composition and layer thicknesses is required for optimizing the microresonator functionally over many iterations. This can be fabricated internally while avoiding delivery times of an external supplier. Another motivation for internal fabrication is the experimental nature of this project. The actual dimensions always differ from the theoretical dimensions due to fabrication inaccuracies that are inherent to fabrication equipment. This means that a process of trial and error is required to achieve the optimal microresonator design which is impractical when relying on external fabrication due to aforementioned reasons.

One very promising candidate for an alternative top layer is amorphous silicon. This can be deposited onto silicon dioxide through chemical vapour deposition. The Kavli cleanroom has an Inductively Coupled Plasma Chemical Vapour Deposition (ICPCVD) machine that is the PlasmaPro 100 from Oxford Instruments Plasma Technology. This machine can deposit both silicon dioxide and amorphous silicon. This has the added benefit that the deposition parameters are constant for both layers so that the adhesion between both layers is optimal. The deposition of the silicon dioxide and amorphous silicon can be executed consecutively.

The use of amorphous silicon as an device layer for ring microresonator is relatively new. This is because the quality of the deposition of amorphous silicon only became sufficient in the last two decades. There are multiple studies that are experimenting with ring microresonators out of amorphous silicon and the results are reasonably optimistic [38, 11, 26]. Furthermore the effective index of amorphous silicon can be tuned to be similar to crystalline silicon and thus studies of crystalline silicon can still be used as an inspiration for fabrication in amorphous silicon.

5.6 Chip layout

The chip will be connected to an optical fiber. This optical fiber will be connected to the waveguide through a glue connection. Henke et al. [27] used a similar connection method to connect the optical fiber to the input waveguide. The waveguide should be as short as possible to minimize the losses of the light as it propagates to the microresonator. Note that in later versions the microresonator will be partially suspended over the edge of the silicon substrate. Leeuwenhoek et al. [32] demonstrated that fabrication of suspended features is possible to an extent. Further experiments should determine how much overhang is possible. The exact dimensions of the waveguide and the microresonator will be determined through simulations in Comsol Multiphysics and Rsoft Synopsys. The grooves to which the optical fibers are mounted will be etched into the silicon substrate according to a study by McKenna et al. [37]. The chip will be mounted in the tip in such a way that the microresonator is in close proximity to the specimen which is situated on the copper grid (Figures 24.a). The shape of the chip is specially designed to fit within the geometric constraints of the tip. The chip is thin at the location of the microresonator since the pole piece separation distance is limited to a couple of millimeters (Figure 24.b).

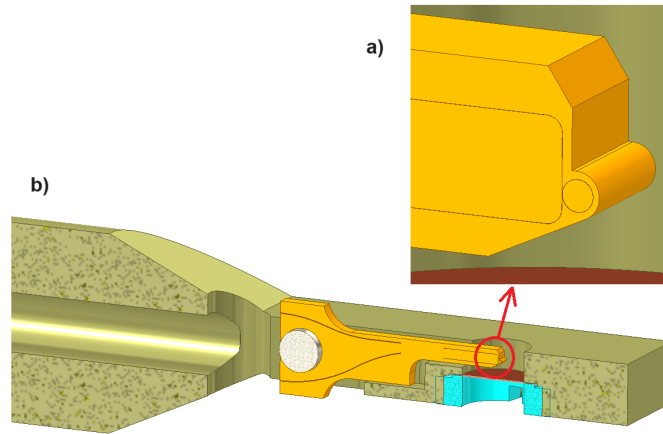


Figure 24: The proposed layout of the chip with a) Zoomed in view of the microresonator in close proximity to the grid, b) Cross section of the tip showing how the chip is mounted.

5.6.1 The grating pattern

A specific optical fiber to waveguide interface is required to transfer the light waves as efficiently as possible from the optical fiber to the waveguide. This interface is a grating pattern that is etched into the device layer of the chip. Most studies glue the optical fiber front face in a 10 degrees angle with respect to the normal vector of the grating plane. This however requires a bend in the optical fiber since the fiber enters the holder along its central axis while it needs to connect to the chip perpendicular to the central axis (as shown in Figure 25). This bend is however very inconvenient since the outer diameter of the tip is only roughly 6.5mm and optical fibers are in general too stiff and fragile to create such a bend. This issue posed a big problem to the design of the tip of the holder. A novel solution to mitigate this problem is one proposed by McKenna et al. [37]. The solution is to polish the face of the optical fiber to a 35 degrees angle. This face acts like a mirror and reflects the waves under a 10 degrees angle downwards into the grating face. This enables the optical fiber to connect parallel to the chip (Figure 26) and thus eliminating the need for a bend (Figure 25). This drastically simplifies the mechanical design and mounting process of the chip into the holder. Micro XYZ stages and real time measurements were used to correctly position the optical fiber with respect to the grating after which glue was applied to fixate the fiber. The grating pattern is a formation consisting of rectangular holes that are etched through the silicon top layer. McKenna et al. [37] estimate that in this way roughly 60 percent of the light is coupled to the waveguide.

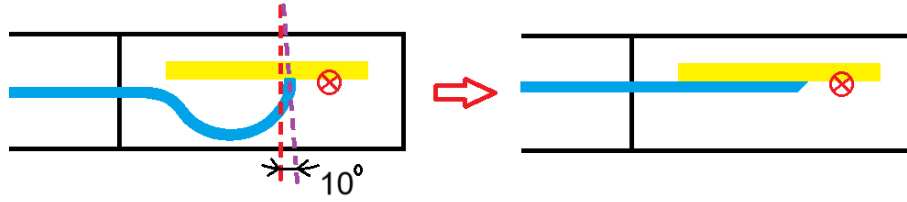


Figure 25: Top view of the holder (along the electron beam axis indicated by a red cross) showing on the left the optical fiber (blue) bend to connect to the chip (yellow) within the holder geometry and on the right the optical fiber connection with a 35 degrees polished face [37].

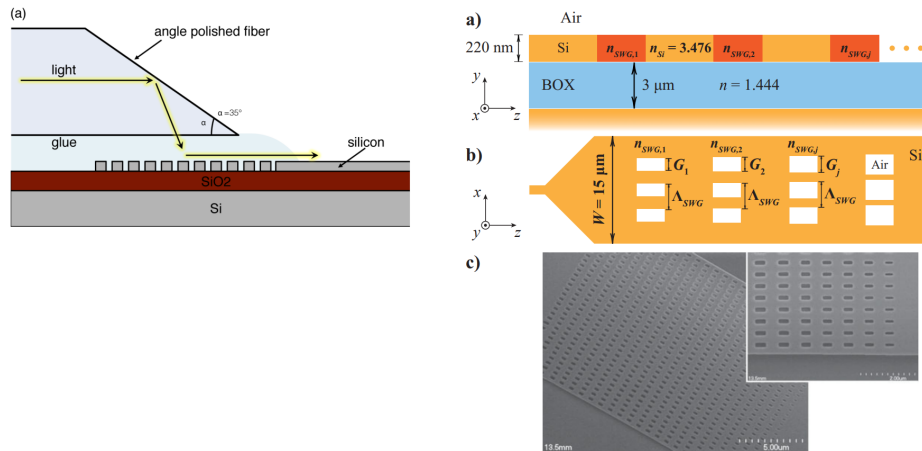


Figure 26: Left) The angle polished fiber that is used by McKenna et al. [37], right) The grating pattern designed by Benedikovic et al. [5] to couple the light from the optical fiber to the waveguide. On the right side: a) layer composition of the chip, b) top view of the grating coupler, c) SEM image of the grating pattern.

6 Electron beam interaction simulations

Nowadays electrons can be regarded as either a charged particle or as a wave. These are two options to simulate the behavior of the electrons. Both options have been investigated in Comsol Multiphysics. However the important question is how to combine the physics of the electrons with the physics of the electromagnetic waves in the resonator. For this a model has been created that combines the ring resonator with the electron beam. The top portion of the ring will be considered since the computation of the coupling between the straight waveguide and the ring in 3D is a costly computation for Comsol. Figure 27 shows what part of the ring resonator has been modelled. It is important to note that the coupling between the straight waveguide and the ring (within the green border) has been left out. Simulations in Rsoft Synopsys have shown that the coupling for the chosen dimensions is sufficient and therefore Comsol does not have to consider this interaction. This significantly reduces the computation load which makes the simulation more robust and less time consuming.

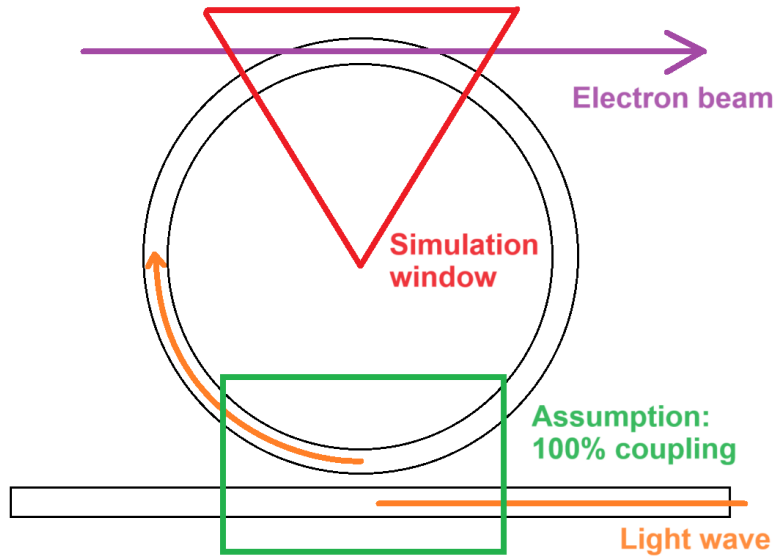


Figure 27: Schematic showing the part of the ring resonator that is modeled in Comsol (within the red triangle).

The optical field with which the electron beam will interact can be seen in Figure 28. The light wave is inserted through the input port consisting of faces A,B and D (as can be seen in figure 29). The output port is defined on opposite faces of the ring segment. It is interesting to note that the mode profile is similar to what has been found in the Rsoft Synopsys simulations (Figure 18). This indicates that Comsol is correctly finding the TM mode for which this ring has been designed. In following sections the simulations of the electron beam and interaction with the ring will be discussed.

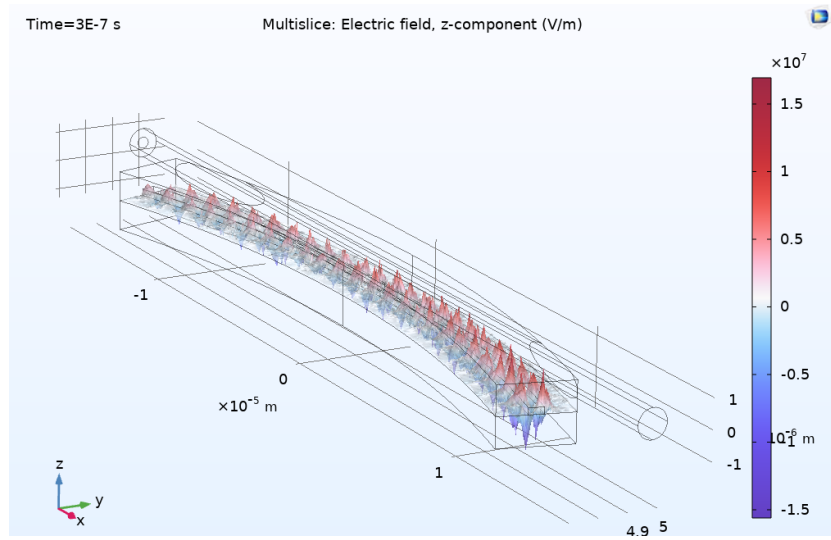


Figure 28: Simulation of the electric field that is generated in the ring segment.

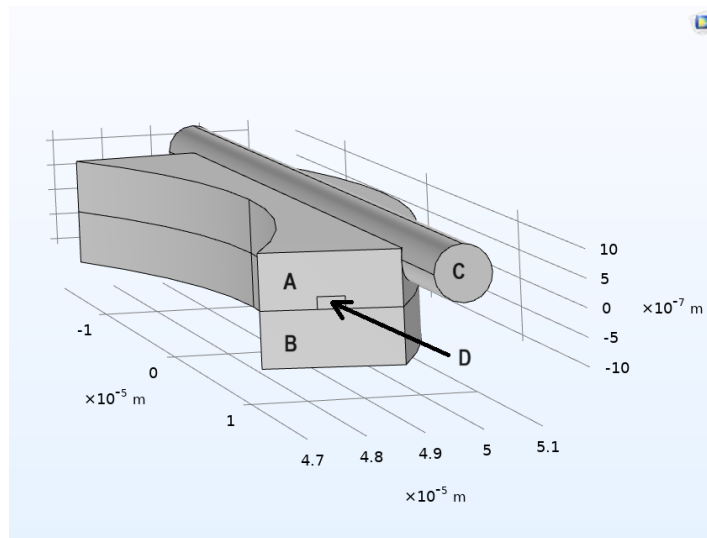


Figure 29: The model that has been created in Comsol Multiphysics according to Figure 27. The ring segments is formed by domains A,B and D while the electron beam domain consists of C. A,C) Vacuum domain, B) Silicon dioxide domain, D) Amorphous silicon domain which is the rectangular waveguide.

6.1 Electron beam simulation as particles

For this simulation a cylindrical domain has been created where a potential difference has been created between both faces. Comsol considers each electron individually as a negatively charged particle. For each particle the resulting trajectory is calculated and traced through the domain. Comsol has a couple of standard modules to simulate particles. The modules that are used are the Electrostatics module and the Charged Particle Tracing module. For each simulation a n number of simulated particles can be set. Figure 30 shows the result of a simulation for $n = 1000$. Note that this simulation is not performed in the aforementioned geometry. For the electron beam simulation in the geometry a smaller number $n = 20$ has been chosen to reduce the computational load while also giving more insight in the trajectory of individual electrons. This simulation can be seen in Figure 32.

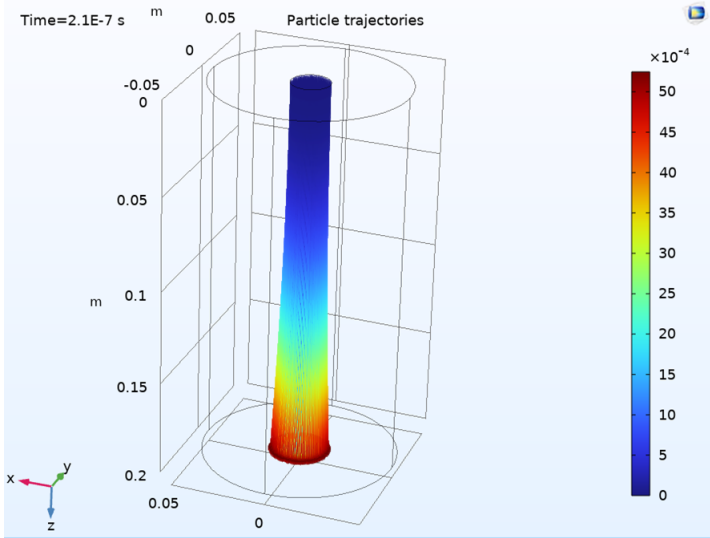


Figure 30: A particle tracing simulation of $n = 1000$ electrons as charged particles as a result of a potential difference. The colors indicate the deviation of the particles with respect to the center line (along the z axis). Red indicates maximum deviation while blue indicates no deviation.

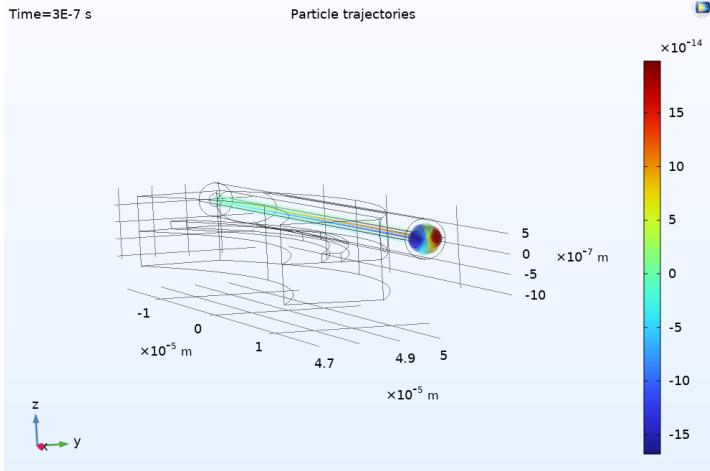


Figure 31: A particle tracing simulation of $n = 20$ electrons as charged particles as a result of a potential difference. The colors indicate the deviation of the particles with respect to the center line of the cylindrical domain (along the x axis). Red indicates maximum deviation while blue indicates no deviation.

6.2 Electron beam simulation as a wave

The Comsol electromagnetic beam envelopes module can be used to simulate a wave that behaves similar to the electron beam inside the electron microscope. This is done in the cylindrical domain (c) that can be seen in Figure 27. This domain can be moved in the z direction with respect to the waveguide (27D) to study the effect of distance between the electron beam and the waveguide.

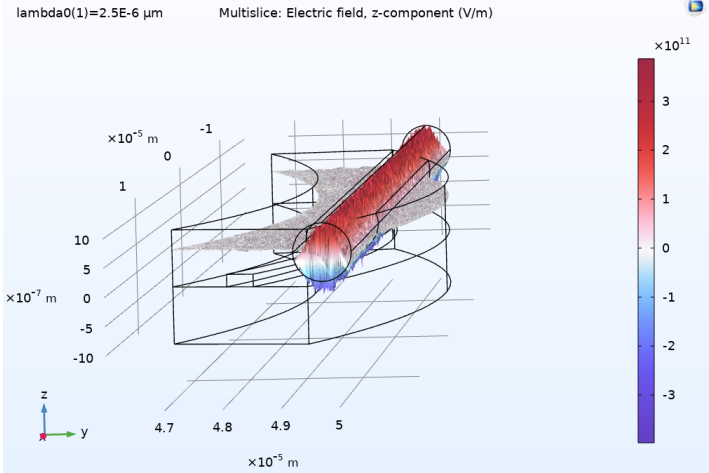


Figure 32: A simulation of the electron beam as a wave using domain c (Figure 27). Both faces of this cylindrical domain have been assigned a port. One port is the "listener port" where the waves are measured and one port is excited with a wavelength of $2.5 \times 10^{-12}m$.

7 Fabrication methods of the TEM chip

7.1 Masks

The MEMS chip will basically be fabricated by adding layers and etching away this layer at desired locations. The removal of layers at desired locations can be done in multiple ways. One way is to add a photoresist layer to a freshly sputtered metallic layer and to imprint a pattern by exposing it to light radiation. There are two basic types of resist namely positive resist and negative resist. A positive photoresist region that is exposed by light will be removed after developing while a negative photoresist region that is exposed to light will remain after developing (Figure 33).

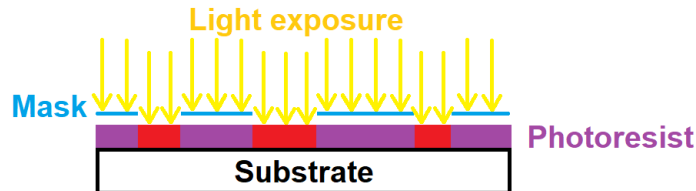


Figure 33: A schematic overview of a positive photoresist versus a negative photoresist. For a positive photoresist the purple region remains after developing and for a negative photoresist the red region remains after developing.

There are multiple kinds of light that can be used to expose, this will be elaborated on later. Depending on whether the photoresist is a positive or a negative resist, certain areas of the photoresist can easily be etched away while other areas of the photoresist are not easily etched away after developing. In this way the photoresist acts like a mask. Another way is by fabricating a plate with the required positive or negative pattern that needs to be exposed. This mask can then be positioned above the wafer after which the photoresist can be exposed through lithography at the desired regions. This however is costly and is only cost efficient when a sufficient quantity of identical wafers need to be manufactured. A third way is to expose the photoresist to an electron beam that can be aimed at (depending on positive or negative resist) regions that need to be removed or maintained. This method has a high accuracy and is very suitable for single chip manufacturing. It is a relatively slow process but it is more cost efficient for single (unique) chip production since fabricating masks for a single chip is very costly. A fairly complex chip can be manufactured by repeating the process of adding layers, removing unwanted areas and adding another layer.

7.2 Deep reactive Ion Etching (DRIE)

Etching will remove the substrate at the regions that are unprotected by photoresist. There are two kinds of etching: dry etching and wet etching. One form of dry etching is bombardment by ions that are generated by a plasma. The selectivity of the etching process is not fully downwards. The etching will also affect the sidewalls of the hole that is formed. This means that the etching process will start to remove substrate from under the resist resulting in a mushroom shaped cavity (which is specially prevalent in wet-etching). This is called under-etching. This effect is undesired when the goal is to form a deep hole with straight side-walls. One way to achieve fairly straight sidewalls and to keep etching downwards instead of sideways is by applying the Bosch process. The Bosch process is a widely used DRIE process in the MEMS industry [10]. The Bosch process starts by etching down into the substrate for a small distance. Then a protective layer is added that covers all the exposed substrate (including inner walls of the hole). The etching is then resumed and the protective layer on the bottom is removed first. Since the etching selectivity is mostly downwards, then the etching resumes into the bottom substrate of the hole. The etching should be resumed until the protective layer on the sidewalls is depleted. Under-etching will also occur during this etching step and thus mushroom shaped cavities will be stacked downwards by repeating this process. This process will result in a hole that is mostly straight down with different under-etching layers (Figure 34). The surface roughness will however be fairly rough but this can be mitigated by a post process that targets the sidewalls. There are extended Bosch-processes that have been investigated including the effect on the losses inside the waveguide as a result of the extended process [21]. The Bosch process can also be applied to produce more complicated structures like micro pillars [10]. Furthermore Bogaerts et al. describe other techniques to reduce the sidewall roughness after the DRIE etching [7].

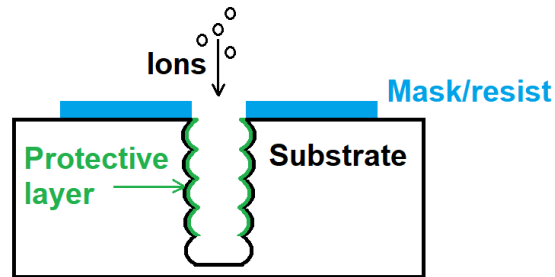


Figure 34: A schematic overview of the cavity formed by the Bosch process. The green layer is the protective layer that is applied after every etching cycle. The blue layer is the mask which contains the desired etching pattern.

7.3 Layer deposition methods

There are two main ways of adding layers to a substrate. One way is physical deposition and the other way is chemical deposition [22]. Physical deposition are for example evaporation and sputtering. Chemical deposition uses a chemical reaction to add a layer of material. Examples of chemical deposition are APCVD (Atmospheric Pressure Chemical Vapour Deposition) and LPCVD (Low Pressure Chemical Vapour Deposition). The cleanroom offers multiple evaporation machines like the FC-2000 evaporation system or the L560 evaporation system. The training however will be done on the AC450 No. 08 sputtering machine from Alliance Concept. A sputtering machine has a vacuum chamber in which a plasma is created. This plasma generates ions that are positively charged. The deposition material is located on the opposite side of the chamber. The deposition material is negatively charged (a cathode). The ions from the plasma will thus accelerate into the deposition material and collide. The collisions free the deposition material atoms and those will scatter across the chamber. During this process the atoms also land on the substrate and build up a layer [42]. Sputtering can be used to deposit metallic layers as well as ceramic layers.

7.4 Acid cleaning

Acid cleaning is a wet etching technique. This process is used to remove layers or contamination. This happens inside of a wet-bench. This is a desk that contains holes in the working surface that allows an airflow upwards. There is a slight under pressure in the wet-bench that prevents toxic fumes from escaping the enclosure of the wet-bench. This air-flow system keeps the handler safe from any dangerous fumes that would be toxic to inhale. The air cleanliness is higher inside a wet-bench than in the surrounding clean room. The contamination of dust particles in the wet-bench is 100 particles (greater than $0.5\mu m$) per square foot and the contamination in the general clean room area is 10.000 particles (greater than $0.5\mu m$) per square foot. The general training in the wet-bench is done with fuming nitric acid (HNO_3). Multiple acids can be used once the final wet-bench test is completed. The type of acid can be determined based on for example the material that has to be removed or based on the desired selectivity. There are experimentally determined protocols for removing the desired thickness of material. These protocols are a strict time schedule and order for the steps of the acid cleaning process in order to achieve the desired result.

7.5 Inspection methods

Inspection is crucial when fabricating small mechanisms with high geometrical tolerances. The critical dimension while applying layers is the thickness. The height is very critical for the effective index in a waveguide. This is why close inspection is important. Furthermore regular inspection must occur to observe that the micrometer structures are in tact after each production step. One way to observe this is by use of an optical microscope. The optical microscope offers a quick way to inspect the surface of a substrate with relative ease. The optical microscopes that are available in the Kavli cleanroom are for example the Olympus bx series microscopes. These are also equipped with a camera to digitally perform measurements on the dimensions of the features that have been photographed. It also has multiple light filters. These can for example be used to prevent over-exposure of photo-resist layers on the substrate.

Another machine that can inspect the features with a larger magnification is the scanning electron microscope (SEM). The SEM can magnify the sample over a hundred thousand times. This can be used to observe nanometer sized features. The SEM uses an electron bundle that can be scanned over the surface of the substrate. The energy levels of the scattered electrons are measured and mapped to pixels to create a grey scale image of the surface. The SEM that is available in the cleanroom is the Nova SEM of FEI.

The height of the applied layers can be measured by an atomic force microscope (AFM). These microscopes map the height profile of features on the substrate through a cantilever beam with a small tip. This tip is pulled across the features and the vertical displacement of the tip results in bending of the cantilever. This bending is measured with a laser that is reflected off the cantilever into a photo-diode. The measurement is then translated into a height profile graph that can be easily interpreted. The AFM that is available in the cleanroom is the Dektak XT advanced Bruker.

8 Chip layer design

This chapter will describe the design process in Klayout. Furthermore the process of the fabrication of the chip and the optimization steps that were performed will be discussed.

8.1 Klayout pattern

Klayout is a software package that allows the user to create layered designs for chip manufacturing. The layered design is required because most features require different etch settings or exposure settings. This distinction cannot be made when the design features are not separated in different layers. Different exposure settings can be assigned to each layer. A layer that contains small features require different dose settings than a layer that contains large features. The full design including all layers is shown in Figure 35. All layers will be elaborated down below.

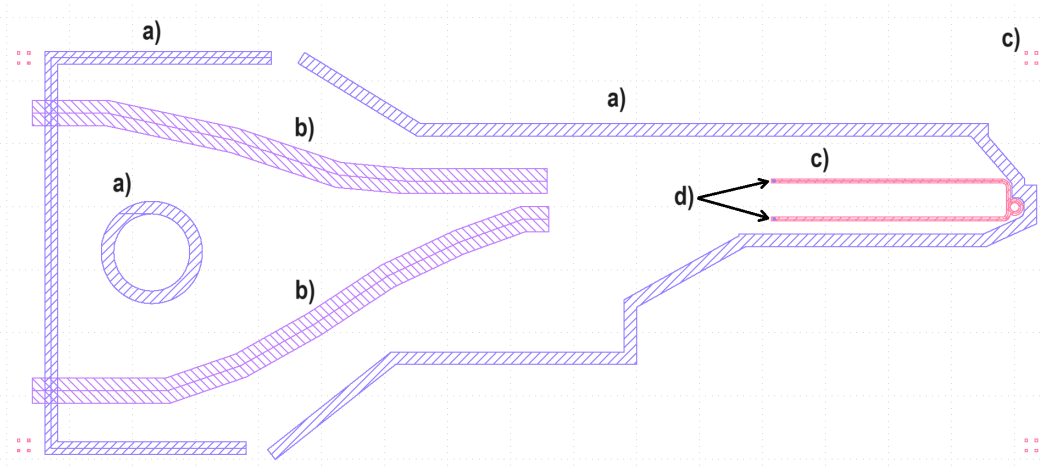


Figure 35: Picture of all the layers of the chip that will be fabricated. There are four layers: a) The contour layer, b) Optical fiber layer, c) Resonator layer + alignment markers, d) grating pattern layer.

8.1.1 Contour layer

The contour layer (Figure 35a) are the features that must be fully etched through the substrate. This includes the external geometry of the chip, that has a special shape to satisfy the geometric constraints in the TEM holder, and the geometry of the hole that will be used to fasten the chip to the holder with a screw. Note that the external geometry is a discontinuous pattern. This allows the chip to remain partly attached to the substrate after etching. Further tests must be conducted to determine how thin these "bridges" must be to break the chip out without damaging the internal features of the chip. This layer requires the chip to be mounted onto a carrier wafer during etching to prevent damage to the machine once the etching reaches the full depth. The pattern for the screw hole is an hollow pattern. This reduces the writing area for the Ebeam machine which reduces exposure time.

8.1.2 Optical fiber layer

The Optical fiber layer (Figure 35b) is the area that will be etched away to form a groove into which the optical fiber can be glued. This groove will be roughly $200\mu m$ deep to fully embed the fiber into the substrate. These grooves will ensure a sturdy connection to the chip such that rough handling of the chip will not easily cause the optical fibers to come lose. The grooves are aligned with both waveguide ends (Figure 35c).

8.1.3 Resonator layer

The resonator layer (Figure 35c) contains the waveguide and the ring resonator. Both are edged in the amorphous silicon top layer (device layer) and has a height of 220nm . Figure 36 shows a zoomed in picture of the resonator layer. The layer is designed in a positive exposure pattern. This means that the area around the features must be exposed in order to create the features. At each end of the waveguide there is a feature that is used to guide the laser light from the optical fiber into the waveguide. Tests have shown that the waveguide and ring resonator can be etched in one single step with the same dose.

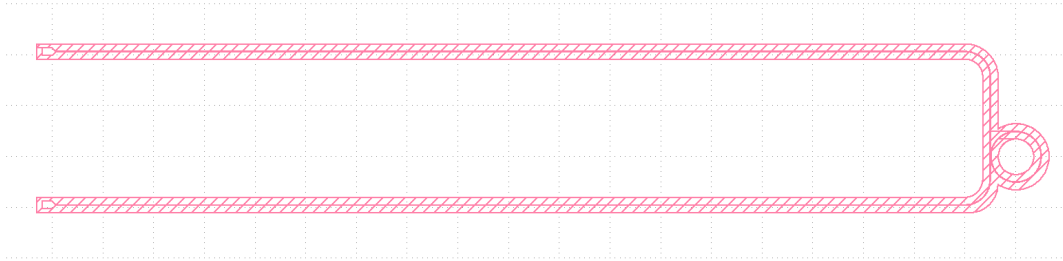


Figure 36: Picture of the resonator layer which consists of the waveguide and the ring resonator.

8.1.4 Grating pattern layer

The smallest feature of the chip layer design is the grating pattern (Figure 37). This consists of an array of tiny rectangles of roughly $400\text{nm} \times 200\text{nm}$. the dimensions of the pad are roughly $15\mu\text{m} \times 25\mu\text{m}$. This pattern is responsible for guiding the light in the Optical fiber to be transferred to the waveguide or vice versa. This layer is separated from the resonator layer because during tests it was observed that the dose of the resonator pattern needs to be higher than the dose of the grating pattern.

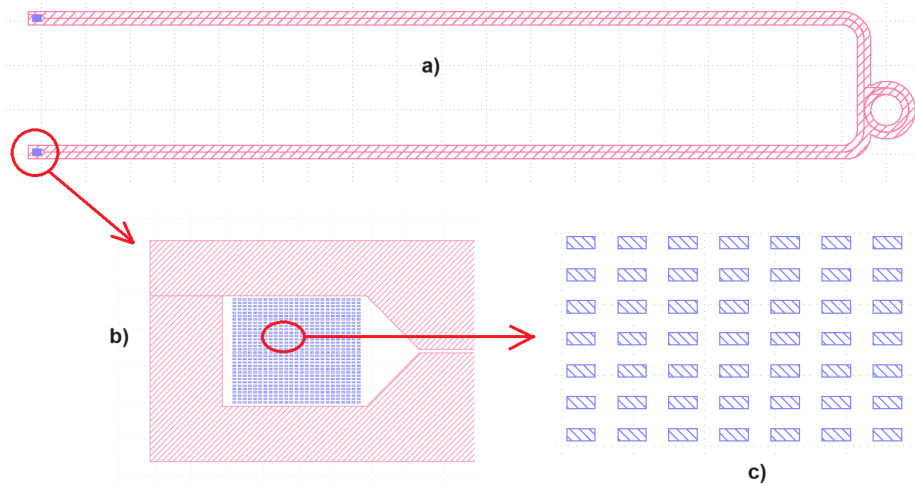


Figure 37: a) Complete resonator layer overview, b) Zoomed in view of the grating pattern pad, c) Zoomed in view of the grating pattern features.

9 Fabrication optimization

This chapter describes the difficulties that have been faced while fabricating the TEM chip in the clean-room. A lot of machines/processes are required for the fabrication of the chip. Each machine/process can be optimized to obtain the best final result. This is however a very time consuming and iterative process with a lot of failure since it is a chain of events that leads to the final result.

The silicon sample is initially cleaned with Ethanol, Acetone and IPA to remove organic contamination. After this the sample is baked to remove water from the surface. In the ICPCVD the silicon dioxide and amorphous silicon are deposited after which the sample is ready to proceed to the following production steps.

The resist (PMMA 950 A6) is now applied on a spincoater after which the sample is baked again to solidify the resist. Then the sample with resist is loaded into the electron beam writer (EBPG5200) where the (positive) resist is exposed. Afterwards the resist is developed in a MIBK and IPA mixture with ratio 1:3. This causes the exposed resist regions to become weak and thus to be removed through etching. In this way the pattern is transferred to the sample.

The etching of the top and substrate silicon layer is done in the Oxford Estrelas at cryogenic temperatures. The etching of the silicon oxide layer will most likely be done in the AMS Bosch etcher since etching of thick silicon oxide layers is not allowed in the Oxford Estrelas. After etching the sample is cleaned to remove the resist that is left over. The remaining resist can be removed by rinsing the sample in Acetone. This process is repeated in order to fabricate all the required layers of the chip. The chip design is divided into layers to produce separate features that require different etching depths and settings.

In the appendix (Chapter 12.1) an alternative production method has been investigated. This method uses UV lithography to transfer the pattern to the resist. The advantage of this method is that the exposure only takes 24 seconds while an equal pattern in the EBPG 5200 would take at least several hours. The downside is that a custom mask has to be fabricated for the pattern which is costly and it limits the ability to iterate on the design.

9.1 Amorphous silicon layer deposition

The selected layer composition is fabricated in the Inductively Coupled Plasma Chemical Vapour Deposition (ICPCVD) machine. First a layer of silicon dioxide is deposited which is approximately $3\mu m$ thick. Secondly a layer of amorphous silicon is deposited with a thickness of approximately $220nm$. Figure 38 shows samples after $3\mu m$ of silicon dioxide and $220nm$ amorphous silicon has been deposited. Both the depositions have been performed at 150 degrees Celsius since usually the layer quality improves as the deposition temperature increases.



Figure 38: Samples with 3 micron silicon dioxide and 220 nm amorphous silicon deposited.

However, some problems were encountered in the consistency of the layers that were deposited. Visual inspection in the optical microscope revealed voids/contamination that can be clearly observed in the top layer of the amorphous silicon. Further tests have to be conducted to determine the cause of this and how to achieve a smooth top layer. These voids transfer to the pattern and are very likely to

compromise the functionality of the microresonator. Due to time constraints the etching tests will be performed on these compromised top layer samples.

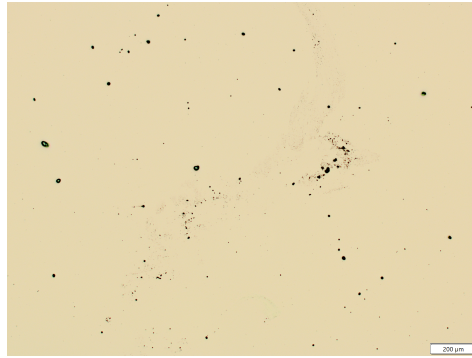


Figure 39: Amorphous silicon layer in which irregularities can be observed.

9.2 Resist

The resist is applied to the sample through a spincoating/ baking process. It is important to determine the correct parameters for the resist to achieve the optimal result. One of the important parameters is the thickness. In general a thinner resist layer will result in a higher resolution pattern since the EPBG beam will more accurately expose the resist with respect to a thicker resist layer. The downside however is that the resist offers less protection to the areas outside of the pattern. The resist should be chosen such that it best compliments the design and fabrication methods.

Initially the samples were created with a negative resist called Hydrogen silsesquioxane (HSQ). A negative resist means that the exposed areas of the resist become very resistant to etching. This means that the entire area that needs to be preserved must be exposed by the electron beam in the Electron Beam Pattern Generator (EBPG). This means that this can be a very time consuming procedure when for example a single hole (which is relative to the entire area very small) needs to be fabricated. For negative resist the entire area around the hole must be exposed while for the positive resist only the area of the hole needs to be exposed. In these cases a positive resist can be a better option. The current design involves a lot of features that are small cutouts in the sample. This is why the decision was made to test out fabrication with the positive resist PMMA 950 A6.

After the exposure in the EBPG the resist must be developed to remove the resist in the exposed areas. The development itself is a process that is done by submerging the sample in a MIBK and IPA mixture with ratio 1:3. The length of the process and the temperature must both be determined experimentally by inspecting the intermediate results through an optical microscope. Initially it was chosen based on similar processes to submerge the sample for 60 seconds at 20 degrees Celsius to remove the resist. It however turned out to be insufficient since the resist was not completely removed in the exposed areas. The sample was submerged for an additional 60 seconds in the developer at 20 degrees Celsius to get rid of the final resist residues. Figure 40 shows the result of resist after development in the SEM.

The development process in PMMA 950 A6 has been optimised by tuning the development time and the dose during the exposure in the EBPG5200. This has been supervised through the optical microscope (figure 41). Note that this sample contains contamination which is responsible for the black dots (as can be seen in figure 39) but it does not affect this experiment. It can be clearly observed that a higher exposure dose results in resist that is more easily removed through developing. This sample has been studied in the SEM afterwards and it was found that a lower dose is more suitable for larger etch surfaces while a higher dose is more suitable for smaller features.

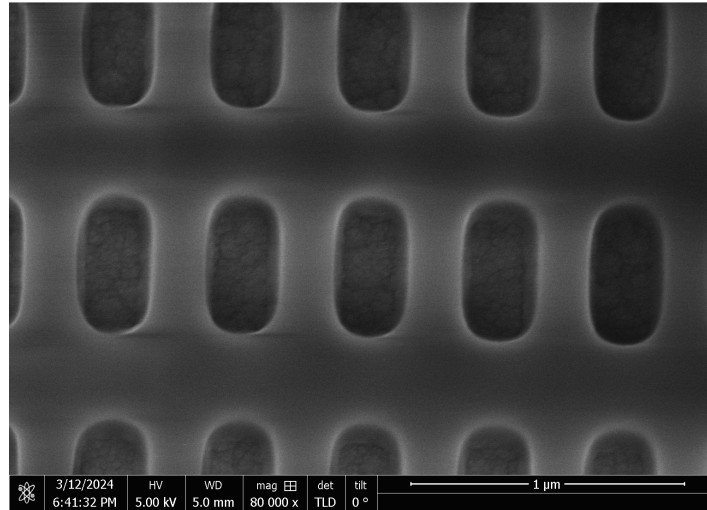


Figure 40: SEM picture of the grating pattern in PMMA 950 A6 resist on top of amorphous silicon after exposure in the EBP5200 and development in MBK:IPA 1:3.

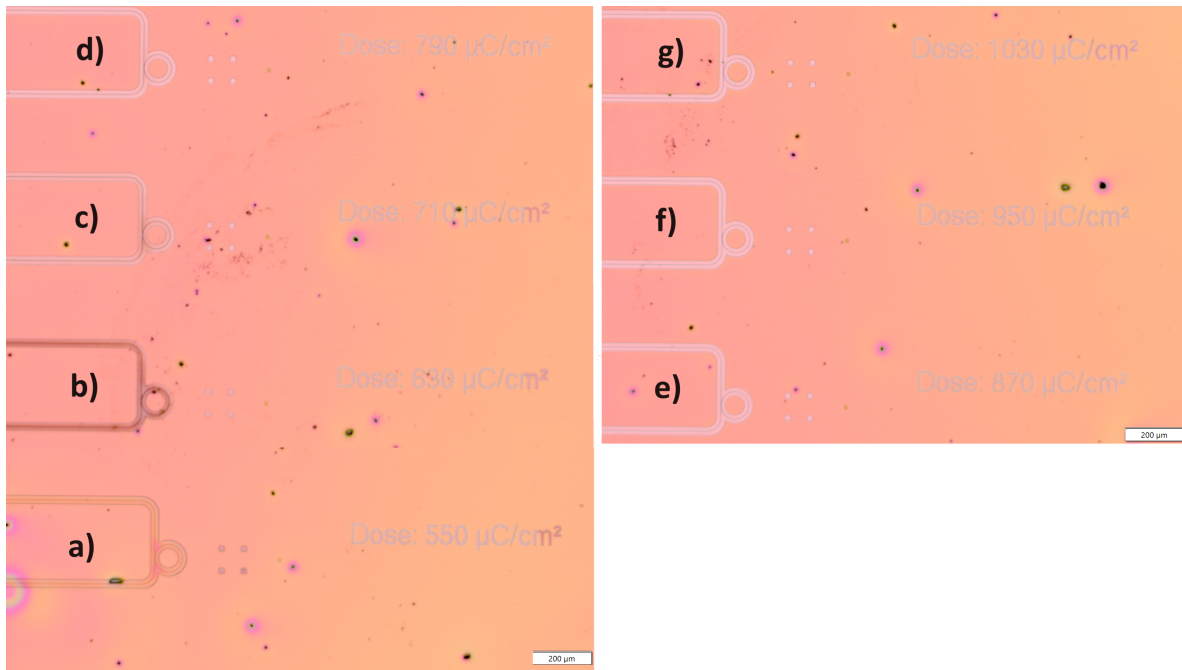


Figure 41: Sample containing a dose update of critical features of the design in PMMA 950 A6 resist after developing the resist with MBK:IPA 1:3. The doses are (in $\mu C/cm^2$): a) 550, b) 630, c) 710, d) 790, e) 870, f) 950, g) 1030. The result after etching can be seen in the appendix in chapter 12.4.2.

9.3 Electron beam writing

The EBPG has multiple parameters that determine how well the pattern is transferred to the resist. A few of these parameters are the beam current, dose, spot size, etc.. For this project it was required to perform tests to determine what the best parameters for the design is. Figure 42 shows a dose test that was performed in order to manufacture a waveguide in silicon. The dose was increased in increments of 100 ranging from 600 to 1100. It shows the influence of the dose on the transfer of the pattern to the resist. Each resist has a threshold dose which means the minimal dose that is required to expose. Too high exposure is possible too which would result in a more "blurry" pattern.

The beam current has a great effect on the writing time in the EBPG5200. The effect of the beam current has been tested out and it was found that the difference between $0.63nA$ and $10nA$ was minimal on the quality of the pattern. The writing time difference was however very significant. The writing time for the $0.63nA$ pattern was roughly 45 minutes while the writing time for an identical pattern with $10nA$ beam current was roughly 10 minutes. This implies that for larger, more inaccurate patterns it might be very time efficient to choose a high beam current. The beam current can be determined through a graph such as can be seen in figure 43. The rule of thumb is that the spot size should be smaller than the smallest feature in the design [39]. The smallest feature size in the design is the width of the holes in the grating pattern which is roughly $120nm$. This means that for an aperture of $200\mu m$ the beam current can be comfortably chosen around $100nA$.

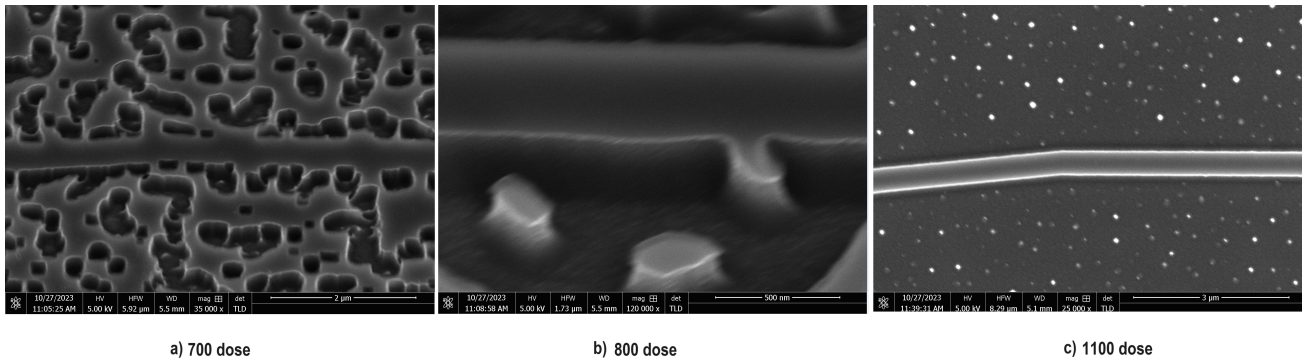


Figure 42: Waveguide pattern etched in silicon with a dose of a) $700\mu C/cm^2$, b) $800\mu C/cm^2$, c) $1100\mu C/cm^2$. Note that the waveguide becomes more defined as the dose increases.

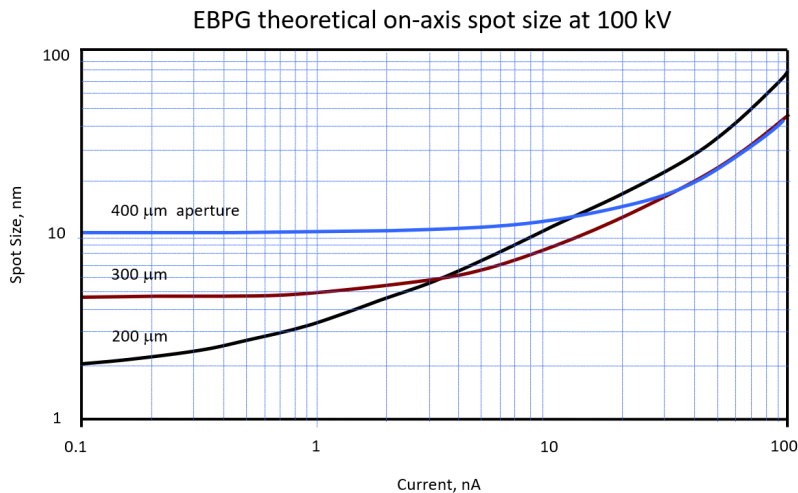


Figure 43: Graph of the relation between the spot size, aperture and beam current settings for the EBPG made by Yale University [39].

9.4 Etching in silicon

Etching tests have been performed in silicon samples to test how well the designed pattern is transferred to the sample. The etching was performed in the Oxford Estrelas in cryo conditions (see the appendix in chapter 12.2.1). Figure 44 shows the first etching attempt of a microresonator in silicon. It must be noted that on that particular day the humidity and temperature in the cleanroom were off due to a technical error. This might explain why the corners show split waveguides since the resist (HSQ) is very sensitive to the process parameter and ages quickly. This effect was not observed in consecutive etching attempts. In the appendix multiple dose tests in silicon can be seen (see the appendix in chapter 12.4.1).

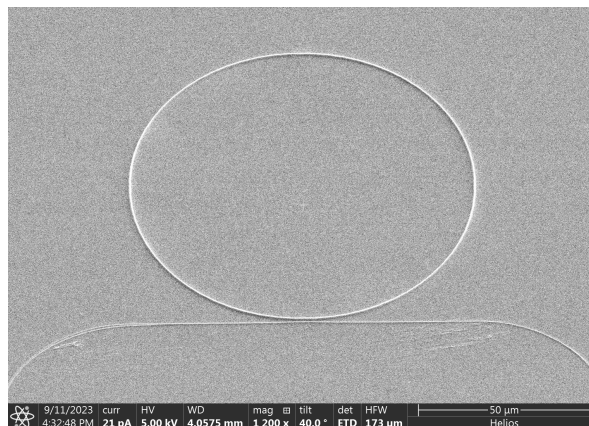


Figure 44: First attempt in etching a ring resonator in silicon.

Etching tests have been performed in the Estrelas for multiple features of the microresonator chip design. This includes the dose markers, grating pattern and the couplers.

9.5 Etching in amorphous silicon

The etching is done in the Oxford Estrelas inside the Kavli cleanroom. The amorphous nature makes the fabrication of straight walled structures more challenging. This is perhaps because there are no crystal borders that would cause the tendency to create straight walls. In the appendix multiple dose tests in amorphous silicon can be seen (see the appendix in chapter 12.4.2).

9.6 Inspection in the NOVA SEM

The inspection of the etching result is done in the Scanning Electron Microscope (SEM). A problem was encountered during the inspection of the sample. A lot of charging was observed while in the immersion mode (figure 45a). The initial assumption was that resist residue might be the culprit. However, after additional acetone cleaning the charging effect still persisted (figure 45b). It was still suspected that resist residue might be present. In order to make sure that no resist residue would be present, an additional nitric acid cleaning (HNO_3) was performed. This time the charging effect was however still present (figure 45c). After all these cleanings resist residues are very unlikely to be present on the sample. After consultation with cleanroom personnel it was determined that most likely the charging is caused by the layer composition of this sample. The sample consists of a silicon substrate followed by a silicon dioxide layer of roughly $3\mu\text{m}$ and finally a amorphous silicon layer of roughly 220nm thickness. The silicon dioxide layer is very thick and very insulating. This most likely causes charge to build up on the surface during inspection with an electron beam.

A way to mitigate the charging effect can be to ground the top amorphous silicon layers so charge cannot build up. Initially it was attempted to ground the sample by clamping it with a copper spring and copper tape (Figure 46). This did not have the intended effect as the charging was still present.

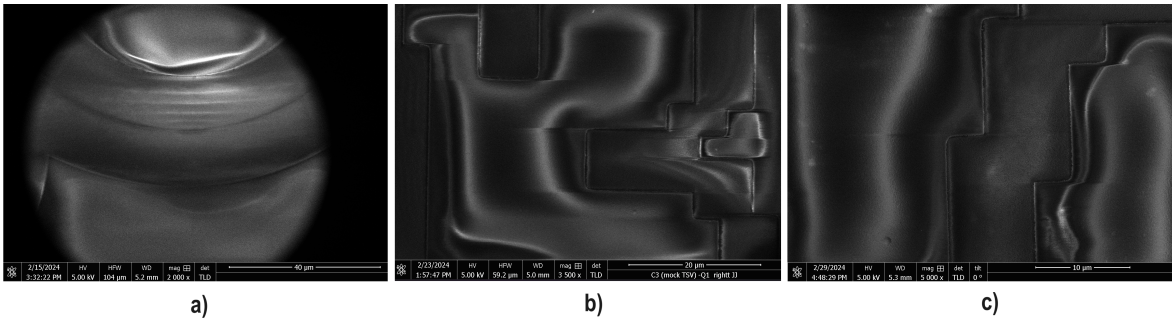


Figure 45: An a-Si sample after etching: a) after regular acetone and IPA cleaning, b) after additional acetone and IPA cleaning, c) after additional nitric acid cleaning.

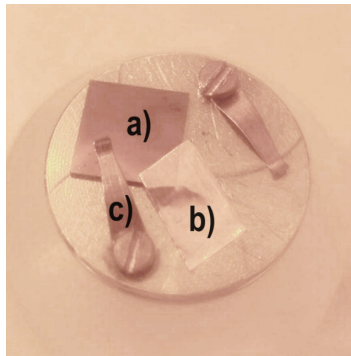


Figure 46: An amorphous silicon sample mounted to a SEM stub with a) the sample, b) the copper tape, c) the clamp.

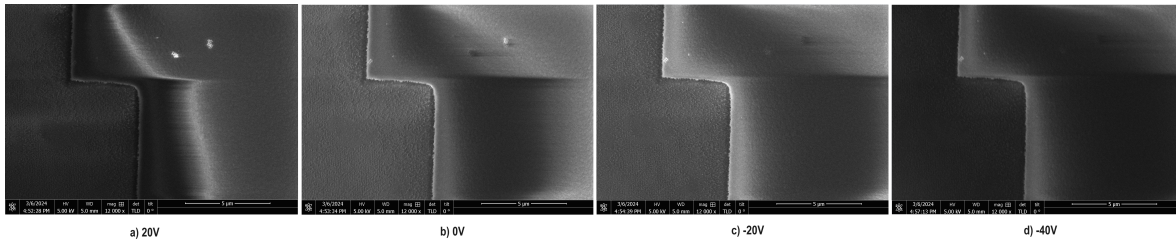


Figure 47: An amorphous silicon sample mounted to a SEM stub (as shown in figure 46) with the detector voltages (20V is the default setting): a) 20V, b) 0V, c) -20V, d) -40V.

Another way to reduce charging is to reduce the beam current. This can be done by reducing the detector voltage. The effect of reducing the voltage on the charging can be seen in Figure 47. The voltage reduction makes the picture darker but a reduction in charging is also observed.

10 Outlook

The possibilities of developing a microresonator inside the TEM holder has been investigated during this project. There is a study which has been mentioned before in this paper by Henke et al. that did investigate how a microresonator can be used to manipulate the electron beam [27]. This study focused on the energy filtering of the electron beam. A possible gap to explore is the possibility of integrating the sample and the microresonator in the MEMs chip or in the same sample holder. Furthermore the location of the sample with respect to the microresonator should be investigated.

The influence of different shaped microresonators can be investigated. There are multiple shapes that are implemented by different studies that each have their own pro's and con's. Heylman et al. show an overview of the performances of different shaped microresonators [28]. Another idea is to partly suspend the microresonator over the edge of the substrate. This greatly reduces the amount of material that is near the electron beam. This reduces charging effects of nearby material that would result in the formation of unwanted magnetic fields that can disturb the electron beam. Finally in later stages a novel idea might be investigated to create a precisely controlled stack of microresonators that is "sandwiched" around the electron beam to generate an even stronger optical field. There is sufficient space available in a TEM holder to facilitate such a design.

There are multiple benefits to implementing both the microresonator and the sample in the same holder. The main benefit would be that energy sidebands of the electron wavepackets can be analyzed after interaction with the sample. The energy filtering of the zero loss peak reveals the sidebands which contain additional information. Furthermore the microresonator would enable researchers to locally limit the dose of the electron beam onto the sample. This reduces the damage to the sample during inspection [31, 15].

Another crucial aspect that needs to be explored is the design of a setup that can be used to position the optical fibers tips on the grating pattern of the microresonator circuit. The optical fibers need to be positioned on a grating pattern of roughly $10\mu m * 20\mu m$ in such an orientation that the light that is coupled to the microresonator circuit is maximized. In this orientation the fibers should be glued to the chip during exposure to uv light. This can most likely be achieved by manually operated micrometer stages under supervision through the optical microscope. Real time measurements of the light coupling must be performed to ensure that the orientation in which the fibers are glued is optimal.

11 Conclusion

This thesis has been written to lay the foundation for designing a microresonator to manipulate the electron beam of a transmission electron microscope (TEM). The design and fabrication of the microresonator TEM holder is a multidisciplinary project with a lot to learn and little examples to lead by. There are multiple difficulties to face such as the simulations, design, fabrication, assembly, testing etc. This thesis attempts to describe the process of investigating these difficulties.

First of all a lot of time has been invested in the simulations (see chapter 5.2, 5.3 and 5.4). Comsol multiphysics has been used to investigate the behaviour of light in photonic structures like the waveguide and the microresonator. Great difficulty has been faced in simulating the coupling between the waveguide and the microresonator in Comsol. Simulations in modes shapes and effective indices have been successful and the Comsol simulations have given insights in the difficulties that need to be faced when designing a ring resonator. Furthermore the electron beam has been simulated in Comsol both as a particle and as a wave. An interaction between the ring waveguide and the electron beam is however yet to be accomplished. The final dimensions of both the waveguide and the ring resonator have been designed in Rsoft Synopsys. The geometry has been optimized such that there is a strong coupling between the waveguide and the ring resonator. The outer diameter of the ring resonator has been chosen to minimize the internal losses.

On the design a lot of progress has been made. The TEM holder has been designed in such a way that the chip can be mounted within the dimensional restrictions of the TEM lenses (see chapter 5.1). A feedthrough for the optical fibers has been integrated in the holder and a mounting mechanism for the TEM grid. The chip has an odd shape to allow for mounting to the tip of the holder with a screw while tapering down to fit between the TEM lenses. The microresonator is aligned very close to the electron beam. This positioning however does not have to be very precise since the holder can be positioned with the use of the goniometer with a range of roughly 1 millimeter in the plane perpendicular to the electron beam. Furthermore the individual layers of the chip has been designed such that it can be fabricated in the cleanroom.

Parallel to the simulations and design of the holder a lot of fabrication has been done in the cleanroom. The focus this far has been on the writing of the pattern in the EBPG5200 and on the etching in the Estrelas (see chapter 9.3 and in the appendix chapter 12.4). The amorphous silicon top layer does enable total control over the layer thickness and refractive index. The difficulty is that there is a lot less experience in the cleanroom with amorphous silicon than with crystalline silicon. This means that most of the fabrication parameters have to be found experimentally which results in a lot of trial and error. One of the difficulties is the different response to etching in the Estrelas. The recipe that would result in straight sidewalls for crystalline silicon creates tapered walls for amorphous silicon.

The project thus far has laid the foundation for the development of the microresonator TEM holder. The designs have been made and simulations have been done to aid the design. Furthermore multiple fabrication tests have been done to test out the optimal parameters.

References

- [1] PP Absil, JV Hryniewicz, BE Little, RA Wilson, LG Joneckis, and P-T Ho. Compact microring notch filters. *IEEE Photonics Technology Letters*, 12(4):398–400, 2000.
- [2] Jessica A Alexander, Frank J Scheltens, Lawrence F Drummy, Michael F Durstock, Fredrik S Hage, Quentin M Ramasse, and David W McComb. High-resolution monochromated electron energy-loss spectroscopy of organic photovoltaic materials. *Ultramicroscopy*, 180:125–132, 2017.
- [3] Paul Azuelos, Pauline Girault, Nathalie Lorrain, Yannick Dumeige, Loïc Bodiou, Luiz Poffo, Mohammed Guendouz, Monique Thual, and Joel Charrier. Optimization of porous silicon waveguide design for micro-ring resonator sensing applications. *Journal of Optics*, 20(8):085301, 2018.
- [4] Brett Barwick, David J Flannigan, and Ahmed H Zewail. Photon-induced near-field electron microscopy. *Nature*, 462(7275):902–906, 2009.
- [5] Daniel Benedikovic, Pavel Cheben, Jens H Schmid, Dan-Xia Xu, Jean Lapointe, Shurui Wang, Robert Halir, Alejandro Ortega-Moñux, Siegfried Janz, and Milan Dado. High-efficiency single etch step apodized surface grating coupler using subwavelength structure. *Laser & Photonics Reviews*, 8(6):L93–L97, 2014.
- [6] Bipin Bhola, Hyun-Chae Song, Hidehisa Tazawa, and William H Steier. Polymer microresonator strain sensors. *IEEE Photonics Technology Letters*, 17(4):867–869, 2005.
- [7] Wim Bogaerts, Roel Baets, Pieter Dumon, Vincent Wiaux, Stephan Beckx, Dirk Taillaert, Bert Luyssaert, Joris Van Campenhout, Peter Bienstman, and Dries Van Thourhout. Nanophotonic waveguides in silicon-on-insulator fabricated with cmos technology. *Journal of Lightwave Technology*, 23(1):401, 2005.
- [8] Wim Bogaerts, Peter De Heyn, Thomas Van Vaerenbergh, Katrien De Vos, Shankar Kumar Selvaraja, Tom Claes, Pieter Dumon, Peter Bienstman, Dries Van Thourhout, and Roel Baets. Silicon microring resonators. *Laser & Photonics Reviews*, 6(1):47–73, 2012.
- [9] CEOS. Omega-monochromator for tem. <https://www.ceos-gmbh.de/en/produkte/monochromators>, 2018. Accessed: 2024-04-18.
- [10] Chienliu Chang, Yeong-Feng Wang, Yoshiaki Kanamori, Ji-Jheng Shih, Yusuke Kawai, Chih-Kung Lee, Kuang-Chong Wu, and Masayoshi Esashi. Etching submicrometer trenches by using the bosch process and its application to the fabrication of antireflection structures. *Journal of micromechanics and microengineering*, 15(3):580, 2005.
- [11] Jun Cheng and Nan Yan. Three-step lithography to the fabrication of vertically coupled micro-ring resonators in amorphous silicon-on-insulator. *Chinese Optics Letters*, 13(8):082201, 2015.
- [12] Raphael Dahan, Saar Nehemia, Michael Shentcis, Ori Reinhardt, Yuval Adiv, Xihang Shi, Orr Be'er, Morgan H Lynch, Yaniv Kurman, Kangpeng Wang, et al. Resonant phase-matching between a light wave and a free-electron wavefunction. *Nature Physics*, 16(11):1123–1131, 2020.
- [13] F Javier Garcíá De Abajo and Andrea Konečná. Optical modulation of electron beams in free space. *Physical Review Letters*, 126(12):123901, 2021.
- [14] RF Egerton and M Malac. Eels in the tem. *Journal of Electron Spectroscopy and Related Phenomena*, 143(2-3):43–50, 2005.
- [15] R.F. Egerton and M. Watanabe. Spatial resolution in transmission electron microscopy. *Micron*, 160:103304, 2022.
- [16] Mustafa Eryürek, Yasin Karadag, Nevin Taşaltın, Necmettin Kılınc, and Alper Kiraz. Optical sensor for hydrogen gas based on a palladium-coated polymer microresonator. *Sensors and Actuators B: Chemical*, 212:78–83, 2015.
- [17] Armin Feist. Ultrafast plasmonics shapes electron beams. *nature materials*, 22(3):280–281, 2023.

- [18] Shaoqi Feng, Ting Lei, Hui Chen, Hong Cai, Xianshu Luo, and Andrew W Poon. Silicon photonics: from a microresonator perspective. *Laser & photonics reviews*, 6(2):145–177, 2012.
- [19] Brent Fultz and James Howe. *The TEM and Its Optics*, pages 59–115. Springer Berlin Heidelberg, Berlin, Heidelberg, 2013.
- [20] M Galli, D Bajoni, M Patrini, G Guizzetti, D Gerace, LC Andreani, M Belotti, and Y Chen. Single-mode versus multimode behavior in silicon photonic crystal waveguides measured by attenuated total reflectance. *Physical Review B*, 72(12):125322, 2005.
- [21] Feng Gao, Sami Ylinen, Markku Kainlauri, and Markku Kapulainen. Smooth silicon sidewall etching for waveguide structures using a modified bosch process. *Journal of Micro/Nanolithography, MEMS, and MOEMS*, 13(1):013010–013010, 2014.
- [22] Murali Krihsna Ghatkesar. Brightspace, Feb 2022.
- [23] Nicole Gleichmann. Sem vs tem, Feb 2020.
- [24] A Gloter, A Douiri, M Tence, and C Colliex. Improving energy resolution of eels spectra: an alternative to the monochromator solution. *Ultramicroscopy*, 96(3-4):385–400, 2003.
- [25] Werner Grogger, Ferdinand Hofer, Gerald Kothleitner, and Bernhard Schaffer. An introduction to high-resolution eels in transmission electron microscopy. *Topics in catalysis*, 50:200–207, 2008.
- [26] Elizabeth Hemsley, Damien Bonneau, Jason Pelc, Ray Beausoleil, Jeremy L O’Brien, and Mark G Thompson. Photon pair generation in hydrogenated amorphous silicon microring resonators. *Scientific reports*, 6(1):38908, 2016.
- [27] Jan-Wilke Henke, Arslan Sajid Raja, Armin Feist, Guan hao Huang, Germaine Arend, Yujia Yang, F Jasmin Kappert, Rui Ning Wang, Marcel Möller, Jiahe Pan, et al. Integrated photonics enables continuous-beam electron phase modulation. *Nature*, 600(7890):653–658, 2021.
- [28] Kevin D Heylman, Kassandra A Knapper, Erik H Horak, Morgan T Rea, Sudheer K Vanga, and Randall H Goldsmith. Optical microresonators for sensing and transduction: a materials perspective. *Advanced Materials*, 29(30):1700037, 2017.
- [29] WA Imbriale, TY Ootoshi, and C Yeh. Power loss for multimode waveguides and its application to beam-waveguide system. *IEEE Transactions on Microwave Theory and Techniques*, 46(5):523–529, 1998.
- [30] Tobias J Kippenberg, Ronald Holzwarth, and Scott A Diddams. Microresonator-based optical frequency combs. *science*, 332(6029):555–559, 2011.
- [31] Silvan Kretschmer, Tibor Lehnert, Ute Kaiser, and Arkady V Krasheninnikov. Formation of defects in two-dimensional mos₂ in the transmission electron microscope at electron energies below the knock-on threshold: the role of electronic excitations. *Nano letters*, 20(4):2865–2870, 2020.
- [32] Maarten Leeuwenhoek, Richard A Norte, Koen M Bastiaans, Doohee Cho, Irene Battisti, Yaroslav M Blanter, Simon Gröblacher, and Milan P Allan. Nanofabricated tips for device-based scanning tunneling microscopy. *Nanotechnology*, 30(33):335702, 2019.
- [33] Matthias Liebtrau, Murat Sivis, Armin Feist, Hugo Lourenço-Martins, Nicolas Pazos-Pérez, Ramon A Alvarez-Puebla, F Javier García de Abajo, Albert Polman, and Claus Ropers. Spontaneous and stimulated electron–photon interactions in nanoscale plasmonic near fields. *Light: Science & Applications*, 10(1):82, 2021.
- [34] Tao Ling, Sung-Liang Chen, and L Jay Guo. Fabrication and characterization of high q polymer micro-ring resonator and its application as a sensitive ultrasonic detector. *Optics express*, 19(2):861–869, 2011.

- [35] Ivan Madan, Veronica Leccese, Adam Mazur, Francesco Barantani, Thomas LaGrange, Alexey Sapozhnik, Phoebe M Tengdin, Simone Gargiulo, Enzo Rotunno, Jean-Christophe Olaya, et al. Ultrafast transverse modulation of free electrons by interaction with shaped optical fields. *ACS photonics*, 9(10):3215–3224, 2022.
- [36] Aviram Massuda, Charles Roques-Carmes, Yujia Yang, Steven E Kooi, Yi Yang, Chitraang Murdia, Karl K Berggren, Ido Kaminer, and Marin Soljacic. Smith-purcell radiation from low-energy electrons. *ACS Photonics*, 5(9):3513–3518, 2018.
- [37] Timothy P McKenna, Rishi N Patel, Jeremy D Witmer, Raphaël Van Laer, Joseph A Valery, and Amir H Safavi-Naeini. Cryogenic packaging of an optomechanical crystal. *Optics express*, 27(20):28782–28791, 2019.
- [38] Jason S Pelc, Kelley Rivoire, Sonny Vo, Charles Santori, David A Fattal, and Raymond G Beausoleil. Picosecond all-optical switching in hydrogenated amorphous silicon microring resonators. *Optics express*, 22(4):3797–3810, 2014.
- [39] M. Rooks. Electron-beam lithography with the raith ebpg part 2: Choosing parameters. [https://nano.yale.edu/sites/default/files/files/ebpg_training_parameters\(3\).pptx](https://nano.yale.edu/sites/default/files/files/ebpg_training_parameters(3).pptx), 2015. Accessed: 2024-03-08.
- [40] Roy Shiloh, Tomas Chlouba, and Peter Hommelhoff. Quantum-coherent light-electron interaction in a scanning electron microscope. *Physical Review Letters*, 128(23):235301, 2022.
- [41] Chantal M Silvestre, Vy Nguyen, Henri Jansen, and Ole Hansen. Deep reactive ion etching of ‘grass-free’ widely-spaced periodic 2d arrays, using sacrificial structures. *Microelectronic Engineering*, 223:111228, 2020.
- [42] Vincent S. Smentkowski. Trends in sputtering. *Progress in Surface Science*, 64(1):1–58, 2000.
- [43] Nahid Talebi. Strong interaction of slow electrons with near-field light visited from first principles. *Physical Review Letters*, 125(8):080401, 2020.
- [44] B.P. van den Bulk. Evg-620 nuv. <https://www.tudelft.nl/tnw/over-faculteit/afdelingen/quantum-nanoscience/kavli-nanolab-delft/equipment/lithography/evg-620-nuv>, 2017. Accessed: 2024-03-26.
- [45] Giovanni Maria Vanacore, Gabriele Berruto, Ivan Madan, Enrico Pomarico, P Biagioni, RJ Lamb, D McGrouther, O Reinhardt, I Kaminer, B Barwick, et al. Ultrafast generation and control of an electron vortex beam via chiral plasmonic near fields. *Nature materials*, 18(6):573–579, 2019.
- [46] Dan-Xia Xu, Adam Densmore, Philip Waldron, Jean Lapointe, Edith Post, André Delâge, Siegfried Janz, Pavel Cheben, Jens H Schmid, and Boris Lamontagne. High bandwidth soi photonic wire ring resonators using mmi couplers. *Optics Express*, 15(6):3149–3155, 2007.
- [47] Yi Yang, Aviram Massuda, Charles Roques-Carmes, Steven E Kooi, Thomas Christensen, Steven G Johnson, John D Joannopoulos, Owen D Miller, Ido Kaminer, and Marin Soljačić. Maximal spontaneous photon emission and energy loss from free electrons. *Nature Physics*, 14(9):894–899, 2018.
- [48] Pierfrancesco Zilio, Elettra Mari, Giuseppe Parisi, Fabrizio Tamburini, and Filippo Romanato. Angular momentum properties of electromagnetic field transmitted through holey plasmonic vortex lenses. *Optics Letters*, 37(15):3234–3236, 2012.

12 Appendix

12.1 Appendix A: UV Lithography method

For this method the EVG-620 NUV has been used. EVG refers to the company that manufactures this machine. NUV stands for Near - Ultra Violet which refers to the ultra violet light source. This is a machine (see Figure 49) that exposes the resist with UV light through a mask (see Figure 48). This mask has been fabricated previously and contains all sorts of geometries that have relevance to the process of fabricating the microresonator chip. For example optical fiber grooves have been included in the mask pattern. Furthermore these tests are conducted to investigate the appropriate parameters for effectively etching through thick silicon layers without the formation of silicon grass.

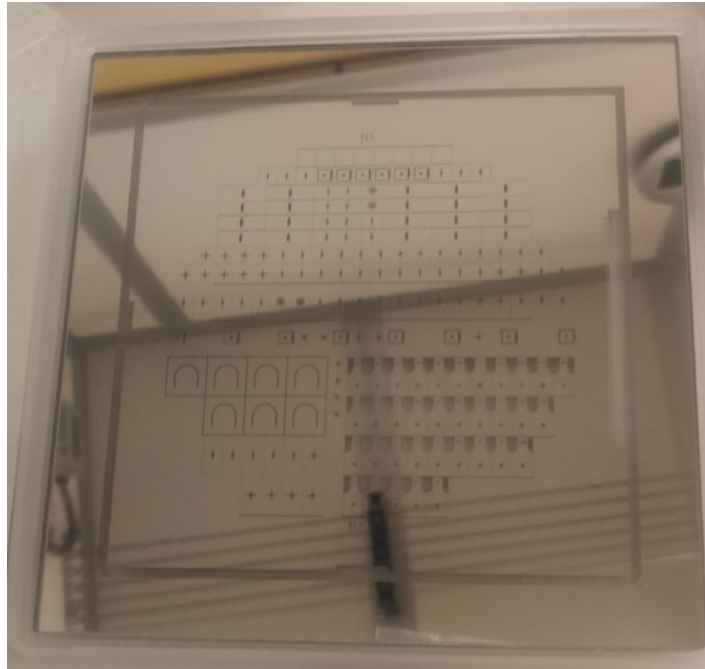


Figure 48: Picture showing the lithography mask that contains the pattern. This mask shields the areas on the wafer that should not be exposed to the UV light.

12.1.1 Silicon grass

The formation of silicon is a problem that has been encountered since it drastically alters the etching rate. This makes the estimated etching time highly unreliable which hinders the ability to stop at a certain depth during the etch. In figure 50 the formation of silicon grass can be observed. There can be multiple causes for the formation of silicon grass. One possible cause is a too high concentration of passivation-gas. This would make sense because it was observed that the formation of silicon grass was less in narrower structures. These structures are less accessible to the passivation-gas and thus less silicon grass will be formed. The structures that had wide open surfaces showed a lot of silicon grass formation. One study that supports this claim is that by CM Silvestre et al. [41]. In this study the effect of sacrificial structures on the formation of silicon grass is investigated. These sacrificial structures reduce the open area of large etching surfaces which in turn reduces the formation of silicon grass.

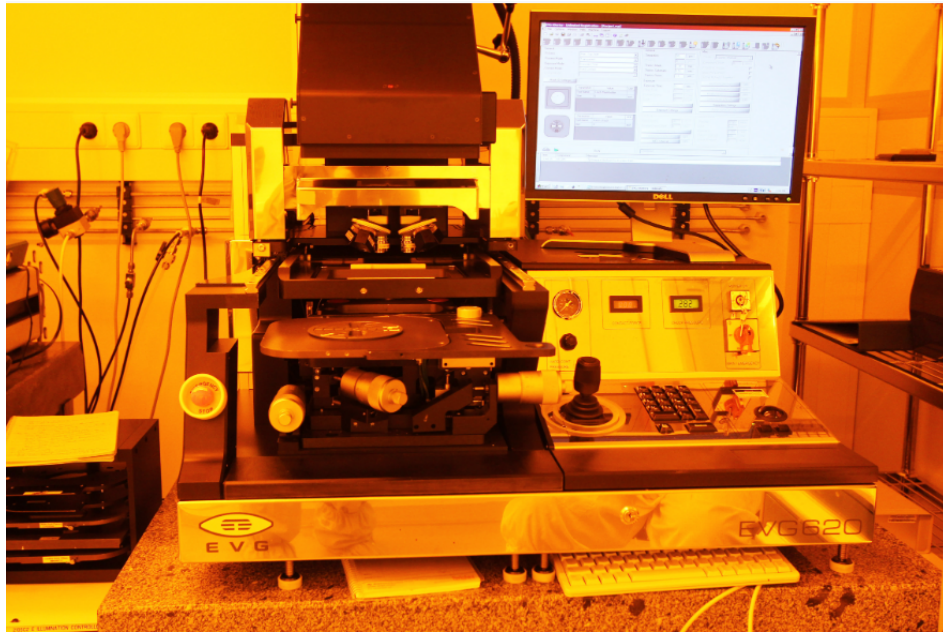


Figure 49: Picture of the UV lithography machine (EVG-620 NUV) in the Kavli cleanroom [44].

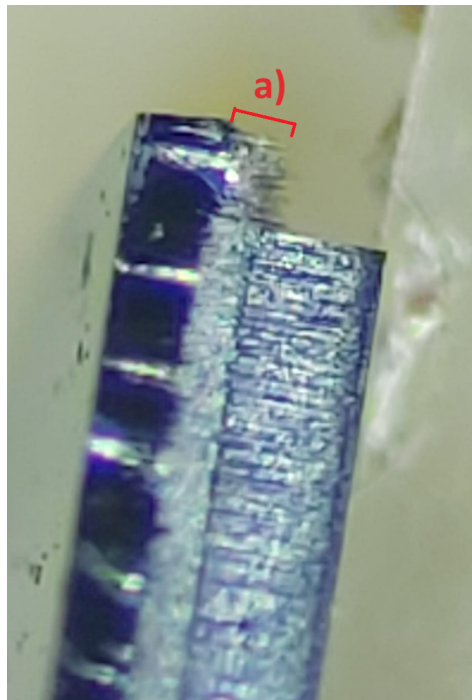


Figure 50: Picture of a cross section of an etched silicon wafer in the Oxford Estrelas with a Bosch process. It can be observed that nearly a third of the depth (designated by region a.) consists of silicon grass (also often referred to as black silicon).

12.1.2 Ebeam pattern generation versus UV lithography pattern generation

Electron beam pattern generation (EBPG) and ultra violet lithography (NUV) are two commonly used methods to transfer patterns to resist layers. Both methods have their advantages and dis-advantages. One major advantage of the NUV lithography is the fact that the exposure time is extremely low compared to the EBPG. For example, the exposure time of the before mentioned pattern is only 24 seconds while a similar exposure in the EBPG could easily take multiple hours. The exposure time of the NUV is so fast because the entire surface of the wafer is exposed to the UV light simultaneously. Areas that are not supposed to be exposed to the UV light are shielded by a mask that is placed between the wafer and the light source. This mask however is the downside of the NUV method. This mask must be specially manufactured for the design which is costly. Furthermore it is very hard to make quick modifications to the mask when certain geometries need to be adjusted in contrast to the EBPG where the writing pattern can be quickly adjusted in for example Klayout. An advantage of the EBPG however is the ability to write at much higher resolutions since the writing is done by a fully controlled electron beam. The resolution of the NUV masks are limited to the manufacturing methods.

12.1.3 AMS Bosch etching

The next deep etching attempt was in the AMS Bosch instead of the Oxford Estrelas. This time the etching surfaces were relatively smooth and no silicon grass was observed (Figure 51b). Both etching wafers have a toplayer of AZ10XT resist of $8\mu\text{m}$ thickness. It can be seen that the resist on the first wafer (Figure 51a) is darker than that of the second wafer (Figure 51b). This is most likely because the resist in (Figure 51a) overheated during the etching which caused the resist to shrivel. The etching settings for the AMS Bosch (Figure 51b) can be found in chapter 12.2.2 and the settings for (Figure 51a) in chapter 12.2.1.

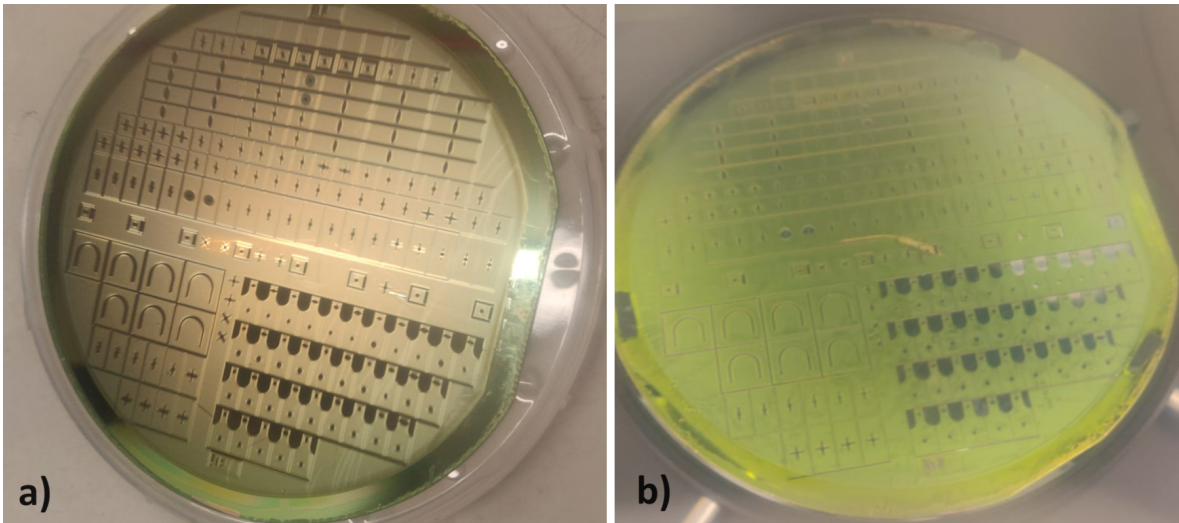


Figure 51: Picture of two different wafers: a) Deep silicon etch in the Oxford Estrelas showing dark etch surfaces consisting of silicon grass, b) Deep silicon etch in the AMS Bosch showing smooth etching surfaces and predictable etching rates.

12.2 Appendix B: Etching settings

12.2.1 Oxfort Estrelas silicon etching parameters

Precise silicon etching recipe in cryogenic mode for smoother sidewalls.

	Parameter	Value
ICP power	Plasma power	500W
RF power	Table power	30W
Duration	Etching duration	40 seconds
Temperature	Table temperature	-120 degrees Celsius
SF6 gas flow	Sulfur hexafluoride	70 sccm
O2 gas flow	Oxygen	30 sccm

12.2.2 AMS Bosch silicon etching parameters

Deep silicon etching recipe with a rate of roughly $5\mu m$ per second.

	Parameter	Value
ICP power	Plasma power	1800W
LF power	Table power	80W
Duration	Etching duration	90 minutes
Temperature	Table temperature	-10 degrees Celsius
SF6 gas flow	Sulfur hexafluoride	300 sccm
C4F8 gas flow	Octafluorocyclobutane	150 sccm

12.2.3 AMS Bosch silicon dioxide/nitride etching parameters

Recipe for etching through silicon dioxide.

	Parameter	Value
ICP power	Plasma power	2000W
LF power	Table power	50W
Duration	Etching duration	-
Temperature	Table temperature	-10 degrees Celsius
CH4 gas flow	Methane	10 sccm
C4F8 gas flow	Octafluorocyclobutane	20 sccm
He gas flow	Helium	100 sccm

12.3 Appendix C: The monochromator

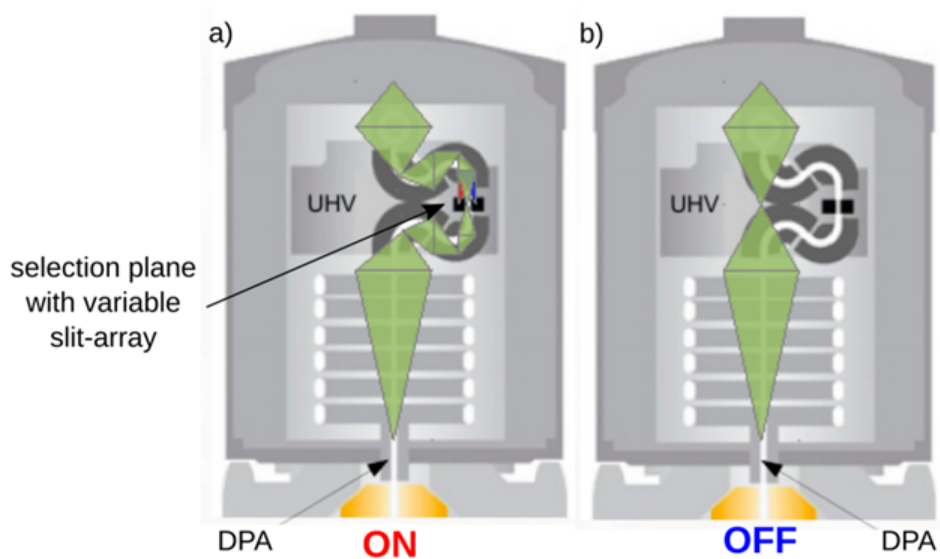


Figure 52: Schematic showing how the electromagnetic lenses in the monochromator diversify the electron trajectory through slits [9].

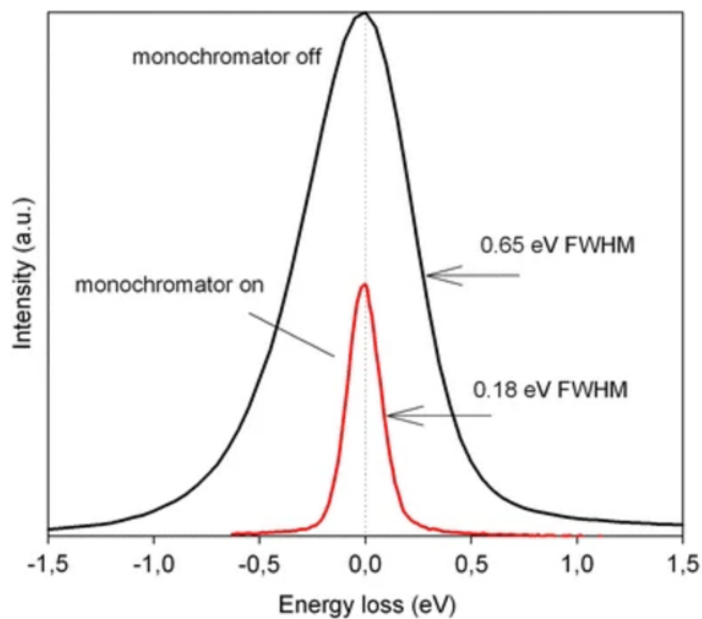


Figure 53: EELS spectrum showing the effects of the monochromator on the full width at half maximum of the zero-loss peak [25].

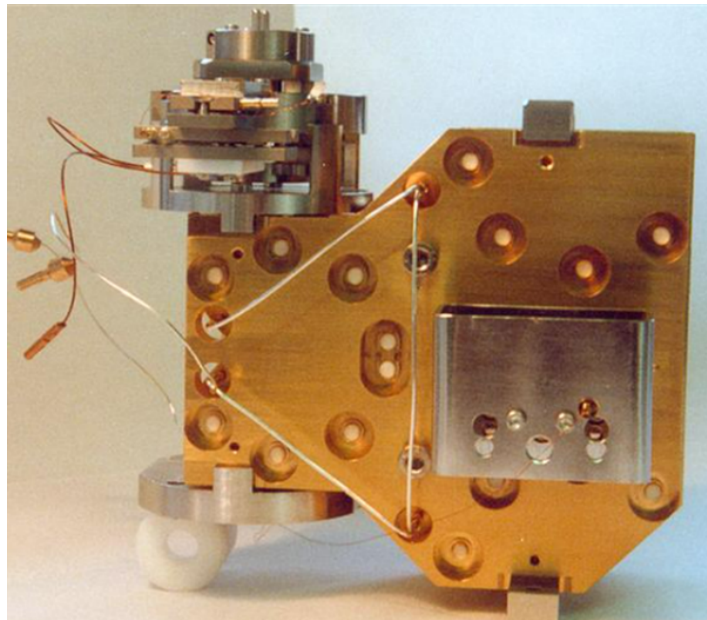


Figure 54: Picture of the monochromator [9].

12.4 Appendix D: Dose update tests

12.4.1 Dose updates in silicon

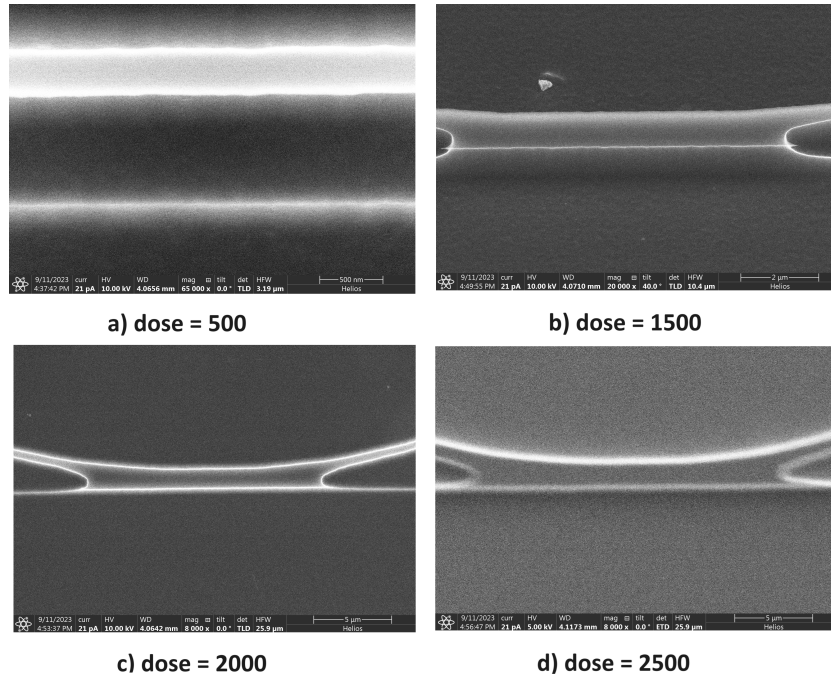


Figure 55: SEM images of dose updates to find optimal dose for the ring and straight waveguide structure in silicon. The structure was made with a HSQ resist. The units of the dose are in $\mu C/cm^2$.

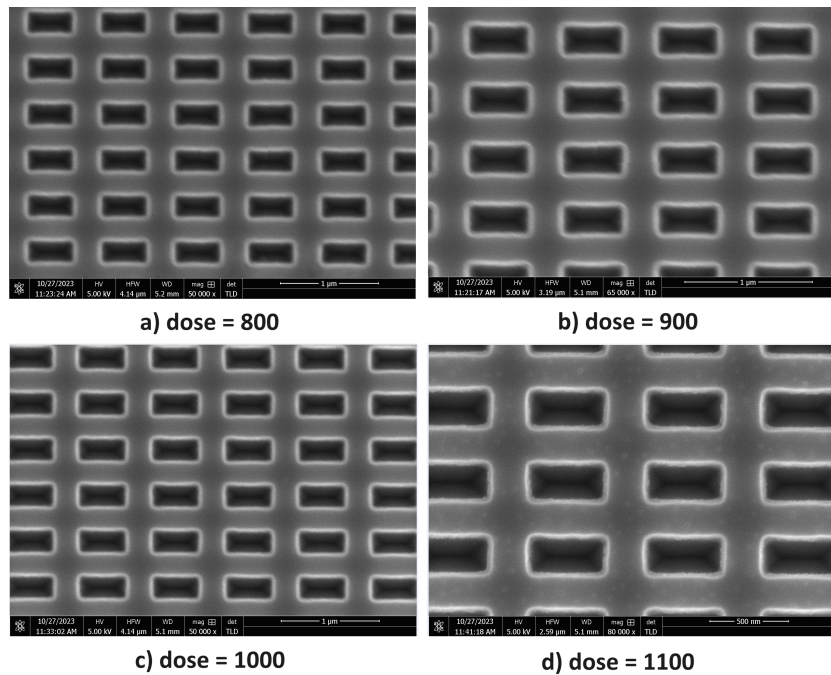


Figure 56: SEM images of dose updates to find optimal dose for the grating pattern in silicon. The structure was made with a HSQ resist. The units of the dose are in $\mu C/cm^2$.

12.4.2 Dose updates in amorphous silicon

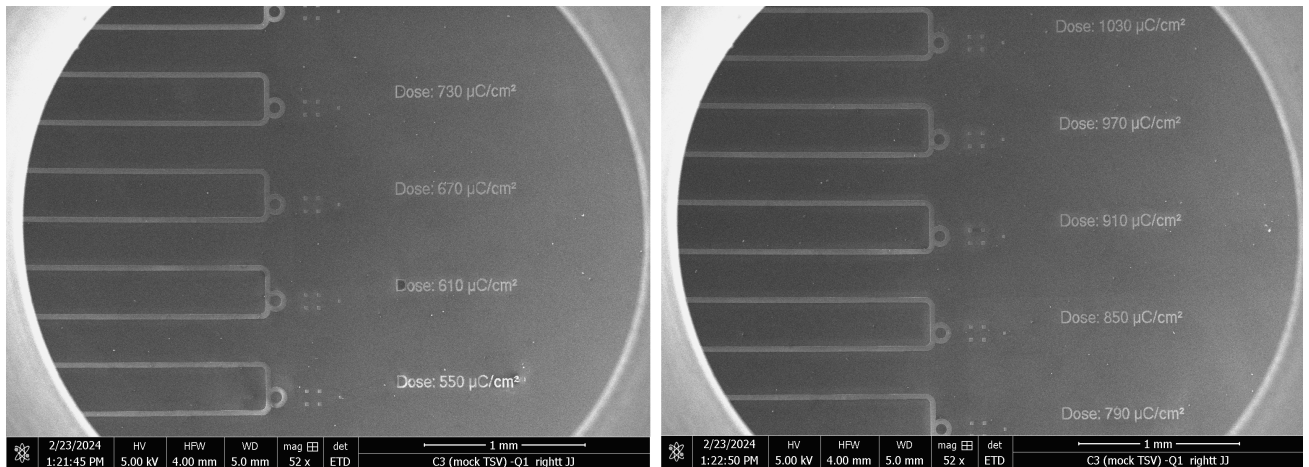


Figure 57: SEM images of dose updates of the crucial features of the design to find their corresponding optimal dose in amorphous silicon with PMMA 950 A6 resist.

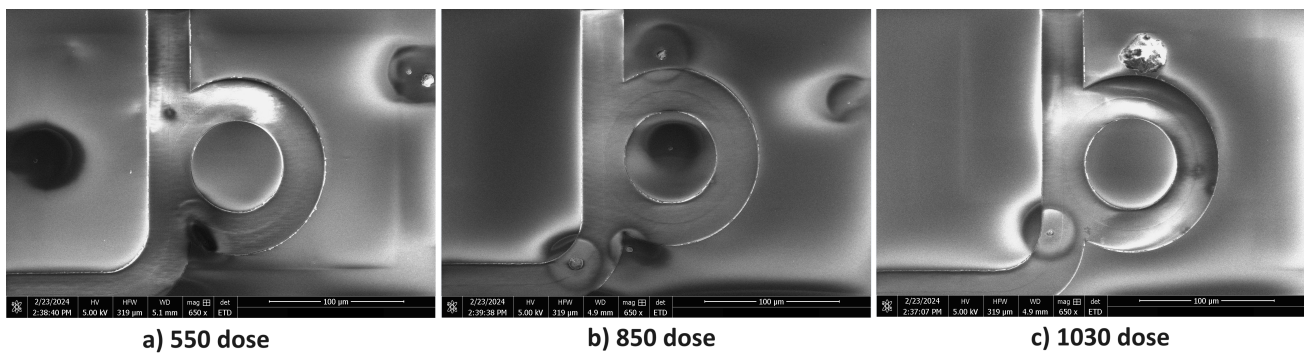


Figure 58: SEM images of dose updates of the ring and waveguide structure to find the optimal dose in amorphous silicon with PMMA 950 A6 resist. Contamination can be observed in the pictures in the form of strange blobs. This is most likely residue from the dicing process. The units of the dose are in $\mu\text{C}/\text{cm}^2$.